TRENDS IN THERMAL DESALINATION PROCESSES

Hisham T. El-Dessouky

Chair professor of altayyar group for water desalination studies and professor of chemical engineering, Chemical Engineering Department,

ALImam Mohammad Ibn Saud Islamic University (IMSU),

Riyadh, Saudi Arabia.

Email address: eldessouky111948@gmail.com

Abstract

Water is life. The availability of sufficient quantity of high quality water for drinking, domestic uses and commercial and industrial applications is critical to health and wellbeing, and the opportunity to achieve human and economic development. Water is becoming an increasingly precious commodity in most of the Gulf States, Australia, China, Japan, the United States, Spain and other European countries, and Caribbean nations. Water desalination industry proved to be a viable and sustainable source for fresh water. In some places, water desalination is the only source for fresh water supply.

Water desalination industry has evolved from a limited number of small-scale desalination units to huge. e production plants. Success of the desalination industry is proved to be a result of continuous research and development and adoption of such developments on industrial. One of the major developments, which proved to have a strong and positive impact on the industry and the unit product cost is the increase in the production capacity of the plant. Searching for better operation and lower production cost, the producers have adopted several other industrial trends; Such as use of heat pumps, use of new material of construction, and inexpensive composites polymers and the decrease the number of pumps. The evaluation also addresses several of the new innovations, which remains to be adopted on industrial scale. Increase in the plant capacity remains to be one of the leading techniques, where technical difficulties in increasing the capacity are approached by innovative solutions. Also, use of heat pumps, such adsorption and absorption cycles, promise to be of very high advantage in enhancing the process performance.

INTRODUCTION

Water is life. The availability of sufficient quantity of high quality water for drinking, domestic uses and commercial and industrial applications is critical to health and wellbeing, and the opportunity to achieve human and economic development. People in many areas in the world particularly in the Middle East have historically suffered from inadequate access to safe water. As a result they suffered heavily from health consequences and have not had the chance to develop their resources and capabilities to achieve major improvements in their standard of living. Example of countries suffering from the fresh water scarcity is the Kingdom of Saudi Arabia. The kingdom is the largest area in the world without a single river. Water is becoming an increasingly precious commodity in most of the Gulf States, Australia, China, Japan, the United States, Spain and other European countries, and Caribbean nations. Also, it is estimates that approximately 20 percent of the world's population live in countries around the globe where water is scarce or where people have not been able to access the resources available [1] . This situation becoming more serious because of the growth of world population, depletion of underground water and the pollution of the natural water resources.

Water desalination or the extraction of fresh water from salt water creates a new water from underutilized impaired sources, provides safe water, ensure the sustainability of the nation’s water supply, keep water affordable, and ensure adequate supplies. It is the only additional renewable source of freshwater available on this planet [2]. The newly released statistics indicate that desalination is playing an increasingly important role in addressing the global thirst for new water resources. In fact,

for many community desalination provides the only reliable supply source for fresh water. At the moment, around 1% of the world's population are dependent on desalinated water to meet their daily needs, but by 2025, the UN expects 14% of the world's population to be encountering water scarcity , Unless people get radically better at water conservation. The desalination industry has a very strong future. It is now practiced in 150 countries [3].

The Kingdom of Saudi Arabia is world's principal producer of desalinated water. Currently, there are 32 water desalination plants in operation, with a total daily production of more than 6 million cubic meters of water. This is the biggest industrial base for desalination in the world . The desalinated water accounts for more than 50 percent of drinking water supply. Additional needs are estimated at six million cubic meters per day of water capacities over the next 20 years due to rapidly growing populations, urban development, depleted ground water resources, greater per capita water demand, and the retirement of capacity built during the oil boom years of the 1970s and early 1980s. About 90% of the desalinated water in the kingdom is produced from thermal desalination plants mainly the Multin Stgae Flashing (MSF) depicted in Figure 1 [4].and the Multiple Effect Evaporation (MEE) Figure 2 [5]. Most of these desalination units are of high capacity and located in the west and east sides of the kingdom. The desalinated water is transported through a very long pipeline systems to the main cities in the kingdom. This add an extra expenses to the desalinated water. Thus, there is a need for innovative solutions to deal with the high cost of desalinated water necessary to develop remote arid areas all through the Middle East. In particular in remote sparsely populated regions of the country where there is an abundance of brackish groundwater.

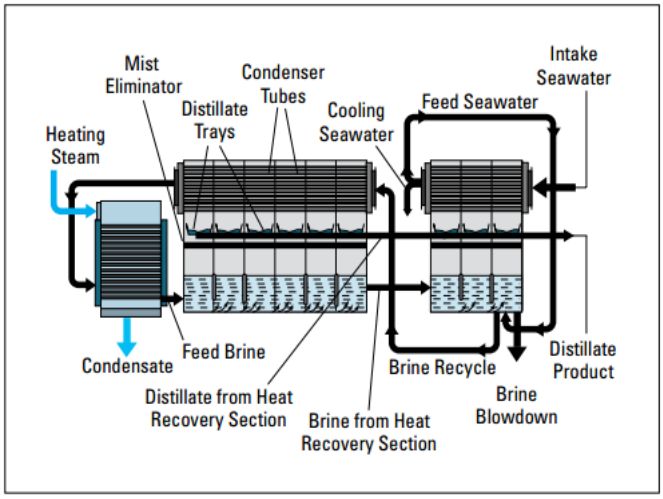

Figure 1. Multistage flash distillation (MSF) desalination.

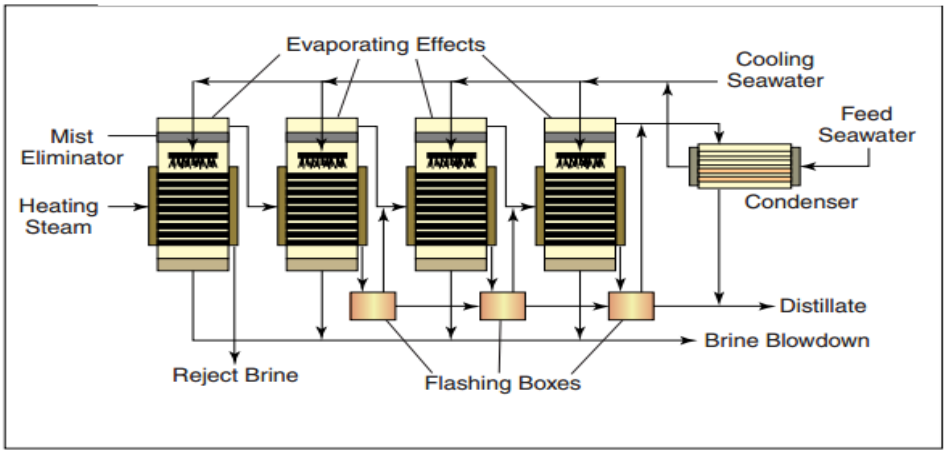

Figure 2. Multiple-effect evaporation (MEE) desalination.

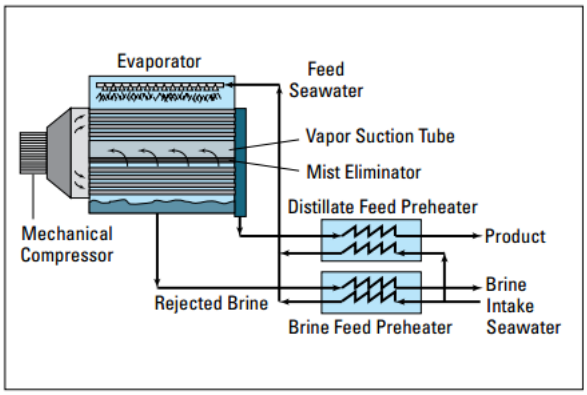

Figure 3. Mechanical vapor compression (MVC) desalination.

The installed base of desalination plants around the world now has a capacity of 78.4 million m3/d (19.8 billion US Gallons) compared to 47.6 million m3/d (12.6 billion US Gallons) at the end of 2008. The past five years has seen a 57% increase in the capacity of desalination plants on-line according to the latest data published by the International Desalination Association (IDA) and Global Water Intelligence (GWI) [6] .

The growth of the market for desalination reflects the fact that coastal communities are increasingly turning to the sea to meet their drinking water needs, while inland there is a tendency for groundwater to become increasingly brackish over time. Historically, large scale desalination has mainly been built in the Gulf region where there is no alternative

Desalination is now practiced in 150 countries, Figure 4 and Table 1 show the top 10 desalinated water producer countries in the world [7].

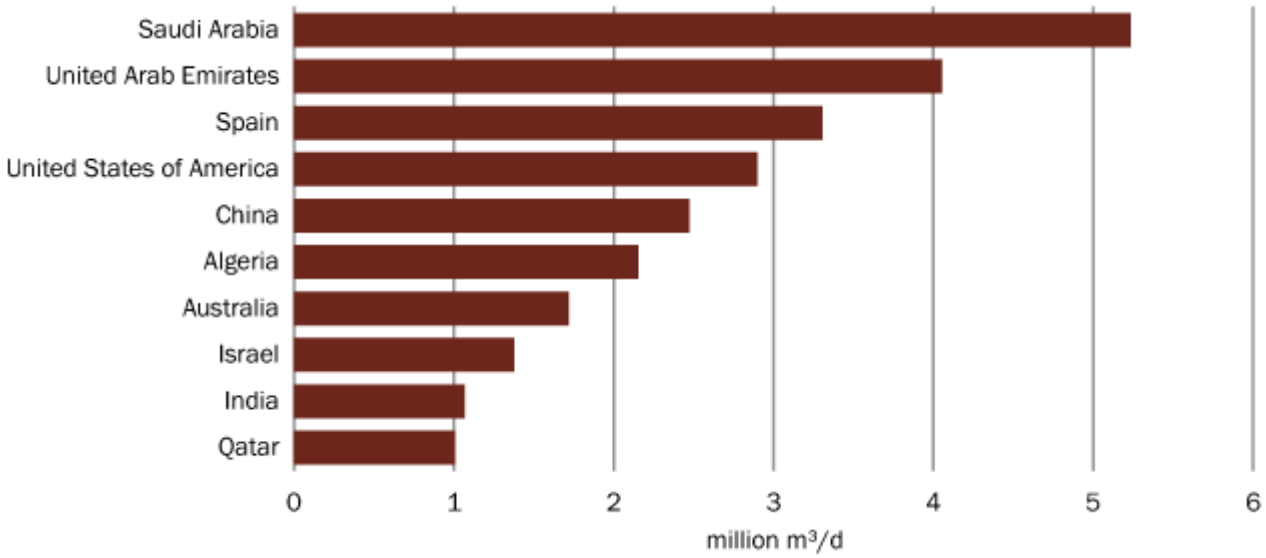

Figure 4 depicts the main producer of the desalinated water.

Table 1, the top 10 seawater desalination countries by online capacity are [7]:

Country	Commissioned seawater desalination capacity m3/d
Saudi Arabia	9,170,391
UAE	8,381,299
Spain	3,781,314
Kuwait	2,586,761
Algeria	2,364,055
Australia	1,823,154
Qatar	1,780,708
Israel	1,532,723
China	1,494,198
Libya	1,048,424

Trends in industry [7 to 17]

Water desalination industry have been developed dramatically within the last sixty years. This expansion is driven by the growth of population, increase in standard of living, depletion of underground fresh water, industrial development and pollution of natural water resources. Moreover, the high rate of decrease in desalinated water cost makes it available for many nations with limited national income. This Progress in desalination depends on many variables such as energy availably and cost and availability of financing.

The following outlines he main development in the thermal desalination industries [8,9,10,11,12,13 and]:

- The first land base plant is the six effect plant with a capacity of 75 m^3/d in 1912 in Al Qwsair, Egypt.
- The total production capacity of the desalination industry increased during the period 1929-1937.
- The four stages flash distillation plant by Westinghouse installed in Kuwait in 1957.
- The patent of Silver in 1957, where the number of flashing stages was close to three.
- The first two MSF plants were installed in Kuwait and Guernsey in UK.
- The first MSF unit was installed in Shwaikh in 1960 with a capacity of 4546 m^3/d, 19stages, and a performance ratio of 4.
- The Point Loma MSF plant with a capacity of 1 migd was constructed in 1962.
- During the sixties plants several achievements have been made, which includes design of MSF plants with capacities up to 25,000 m^3/d or the 6 migd.
- A 12.5 performance ratio MSF plant, largest know for MSF, was constructed in the channel Islands with a 1.5 migd capacity, in two decks, and 40 stages.
- Between 1959 and 1970, the unit capacity was below 4,546 m^3/d. During the 1970's, the unit capacity increased rapidly from values below 4,546 m^3/d to the more standard capacity of 27,276 m^3/d, which operates at a top brine temperature of 90 ^oC.
- The first 27,276 m^3/d MSF units appeared in 1978 and were manufactured in Japan.
- After 1980, the 27,276 m^3/d unit capacity dominated the field.
- During the seventies, more well defined set of plant specifications for construction, operation, chemical treatment, corrosion prevention, and control were compile.
- During the same period, the Japanese manufacturer emerged as a major power in construction of MSF plants. Large number of 22,500-25,500 m^3/d or 6-7.2 migd MSF plants were constructed during the seventies in the Gulf.
- Currently, the largest single desalination plant in operation is the first 1,000,000 m3/d plant is in operation at Ras AlKhair MSF plant in Saudi Arabia.
- The largest thermal desalination plant in the world is the 880,000m3/d Shoaiba 3 desalination plant in Saudi Arabia,

- although this will be displaced in 2014 as the largest desalination plant in the world by the 1,025,000m3/d Ras Al Khair project in Saudi Arabia, which uses both membrane and thermal technology.

- Industrial applications for desalination grew to 7.6 million m3/d for 2010-2013 compared with 5.9 million m3/d for 2006-2009. Of the 7.6 million m3/d, the power industry accounted for 16%; oil & gas, 12% (up from 7% from 2006-2009); mining & metals, 11%; refining & chemicals, 11%; electronics, 5%; and food & beverage, 3%. Other industrial applications accounted for the remaining 40%.

- The largest thermal desalination plant in the world is the Ras Alkhair with a capacity of 1000,000 m^3/d followed by 880,000m3/d by Shoaiba 3 desalination plant in Saudi Arabia.
- At the moment, around 1% of the world's population are dependent on desalinated water to meet their daily needs, but by 2025, the UN expects 14% of the world's population to be encountering water scarcity.
- Global installed desalination capacity is expected to grow by about 55 million m^3/d over the period 2010-2016 at a compound annual growth rate of more than 9%. The estimated cumulative spending is about $87.8 billion during the same period.

- Saudi Arabia and UAE combined will comprise about 14 million m^3/d of desalination capacity over that period.

Increasing the Unit Capacity [18,19 and 20]

For the MSF units, the capacity has increased from low values of 2,273 m^3/d in 1957 to current values varying from 27,276 m^3/d to 57,735 m^3/d. From 1957 to 1965, the capacity varied between 2,273 m^3/d and 4546 m^3/d and the number of stages was limited to 19. Subsequently, the capacity was doubled to 9,092 m^3/d in 1968 and to 18,184 m^3/d in 1970. The current conventional capacity that varies from 27,276 to 32,732 m^3/d has appeared first in 1985-1986. This capacity remains to dominate the MSF market, however, units with 57,735 m^3/d capacity appeared in 1996 and were installed in UAE. A similar trend is also found in the capacity increase of the SEE and MEE processes. For example the first MVC unit capacity varied from 50-500 m^3/d in the early eighties. Today, the industry standard varies between 3000 m^3/d to 5000 m^3/d. Similar increase has occurred in the multiple effect evaporation where the production capacity increased from 500 m^3/d to 12,000 m^3/d.

Development of high temperature freezing process.

Advantages of the high temperature freezing process are [21, 22 and 23]:

1. The operation at a higher temperature than a conventional freezing process, potentially decreases the energy requirements of the plant. However, it would also probably operate at a higher pressure.

2. The higher temperature operation of the gas hydrate freezing process results in a reduction in the amount of compressor work that is required relative to the SRF process.

4. Clathrate desalination now offers the promise of reducing power consumption by a factor of 37, while not significantly increasing the cost of the plant.
.
5. The unit can be produced locally with available materials of construction.

6. The process does not consume chemicals to control the scale formation or foaming. These chemicals are imported from the foreign markets.

7. The process does not pollute the sea or the underground water by dumping harmful chemicals with the rejected brine.

8. The cost of the desalinated water by this process is about US$ 0.8/m^3 . This is 50% and 70% of the costs of the water produced from the large capacity MSF and RO plants, respectively. It is estimated that the cost of desalinated water at remote areas by other technologies is aboutS$ USA $ 4/m^3.

9. Expenses of the electric power less than 100 J/kg per a product.

10. Tolerance to the dissolved substance level in initial sea water or wastewater.

11. Cost of the freshened water at level 1.5-3 $/$m^3$.

12. High quality of the freshened water.

Trends in cost of desalinated water [24,25,26,27,28,29 and 30]

The cost of desalinated water depends on many parameters such as :

- Desalination technology.
- Construction date
- Salinity and quality of feed water.
- Plant capacity:
- Site conditions:
- Qualified labor.
- Energy cost:
- Plant life and amortization

It is worth mentioning that he cost of desalinated water cited in the literature is differ considerably from one plant to other having the same capacity and technology as shown in Table 3 for the mechanical vapor compression units and in Table 4 for the MSF plants with different capacities. The error in cost reported ranges of ±10 to 50%.

Table 3: Cost data for the MVC system

Reference	*Capacity, m3/d*	*Capital cost,US$/ m3/d*	*Power cost, US$/m3*	*Chemical cost, US$/m3*	*Water cost, US$/m3*
Matz&Fisher,1981	1000	894	0.52	0.02	***1.51***
Darwish&AlNajem,1987	750	N/A	N/A	N/A	***0.89***
Darwish et al,1990	100	N/A	N/A	0.05	***5***
Leitner,1992	4000	N/A	N/A	N/A	***2.48***
Zimmerman,1994	20000	N/A	0.41	N/A	***0.46***
Veza,1995	500	1322	1.057	N/A	***3.22***
Morin,1999	4546	N/A	N/A	N/A	***2.43***
Ophir&Gendel, 1999	3000	N/A	0.45	0.03	***N/A***
Ettouney& El-Dessouky,2002(theoretical)	N/A	1000	0.35	0.025	***0.5***

Table 4: Effect of MSF plant capacity on the desalinated water costs

#	capacity	Cost/m3
1	**Less 1000**	**1.78 - 9**
2	**1000 - 5000**	**0.56 – 3.15**
3	**12000 - 60000**	**0.44 – 1.65**
4	**Higher 60000**	**0.505 - 1.00**

The available cost of desalinated water shown in Figure 4 depicted the following:

- At the start of the desalination industry at sixthtess, the cost of desalinated water was about 10 US$/ m3.
- As late as 1975, seawater desalination costs being about US$ 4.10/m3
- Tremendous decreases in desalination costs were continuously achieved in the last decades causing the water price to reach below US$1.00/m3 for MSF.

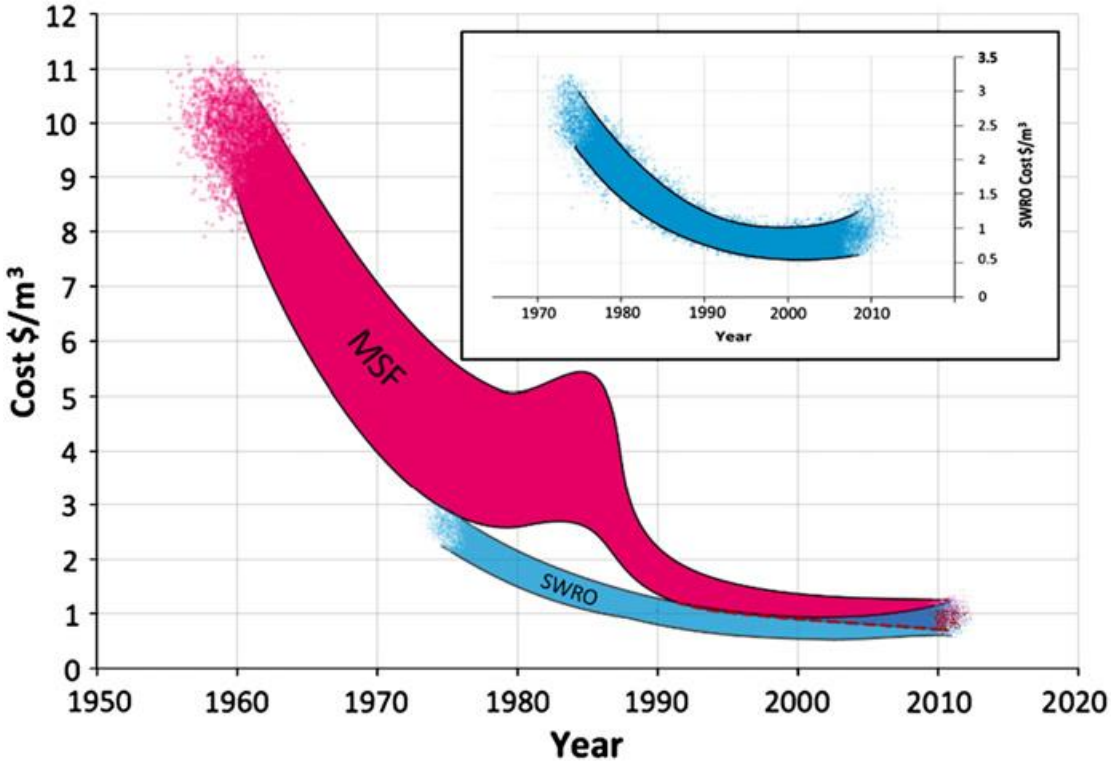

Figure 5: The development in desalinated water costs

Oct. 14, 2013 -- According to new data from the International Desalination Association, the amount of new desalination capacity expected to come online during 2013 is 50 percent more than last year's total. Desalination plants with a total capacity of 6 million cubic meters per day (m3/d) are expected to come online during 2013, compared with 4 million m3/d in 2012.

Trends in Materials [31, 32, 33 and 34]

1. Use of plastic heat transfer tubes

Currently, the heat transfer surfaces in thermal desalination units are made from metallic materials. The most widely used metals are the copper Nickel alloys, titanium, aluminum and duplex stainless steel. Heat transfer tubes account for about one-quarter of the total capital cost for the MSF and MEE units. However, the contribution of the metallic tubes costs in desalinated water expenditure goes up because of the depletion of natural resources for metallic materials, increase demand for metallic tubes, and the lengthy delivery time and high rate of corrosion in sea water environment. A promising and innovative approach is the make use of the nonmetallic materials as a materials of construction for the heat transfer tubes in thermal desalination units. The candidate nonmetallic materials include: high thermal conductivity composite polymers, carbon nano composite, ceramic materials. Nonmetallic heat transfer surfaces have several advantages in comparison to metals:

- Plastics are inexpensive; for example it is five times cheaper than carbon steel and 20 times cheaper than stainless steel. It is shown that the cost of the plastic units is 33%-66% of the conventional metal systems .
- Plastics are highly resistant to chemical attack by acids, oxidizing agents, and many solvents.

- The plastic surface can withstand mechanical erosion, which permits higher fluid velocities inside the tubes. Even if erosion occurs, chemical attack or corrosion of the eroded surface will not take place, which is the opposite to metal erosion.
- The higher chemical resistance of the plastic materials would allow for operation at higher top brine temperatures, i.e., 120 ^{o}C, which would reduce the specific heat transfer area and permit use of acid cleaning.
- Plastics are 4 to 5 times lighter than metals with a density average of 900-2200 kg/ m^3. This reduces transportation, construction, and installation cost.
- Also, plastics are much simpler to shape, form, and machine. This would reduce construction cost and use of highly skilled labor.
- During vapor condensation the smooth surface of the plastics have lower wettability, which promotes drop wise condensation rather than film wise condensation found in metals. Therefore, the heat transfer coefficient for the vapor side in plastics is higher than that for metals.
- From an environmental point of view, the energy consumed for production of a unit mass of plastics is two times lower than common metals, i.e., stainless steel or aluminum. This is an important feature, which conserves the consumption rate of fossil fuels and limits the emission rates of green house gases and air pollutants.

On the other hand the drawbacks of plastics are .

- The thermal expansion of plastics is ten times higher than metals, which necessitate special design considerations.
- Selection of plastic materials should take into consideration the aging properties, which are enhanced by operation at higher temperatures.
- Use of plastic heat exchangers is restricted to a relatively low temperature range of 50-200 ^{o}C.
- Lack of field experience and testing data.

2. Use of date palm lufa fiber in demister [35]

The wire mesh mist eliminator is one of the most important components in the in the thermal desalination units. It is used to improve the quality of the desalinated water and to protect the condenser tubes. Normally, it is made of Nobile metals to withstand the very harsh conditions in the flashing stages. The main advantages of the date palm fiber are: very cheap, available in a massive amounts in the Kingdom of Saudi Arabia, light in weight which decreases the mechanical structure of the flashing stages, maintenance free, because it can be replaced with new fiber with nearly free cost . , It consists of fiber of different diameters which can improve the separation efficiency of the demister, can resist any chemical attack and can be easily shaped for any configuration. Figure 4 shows the demisters made of stainless steel (industrial unit) and the date palm lufa.

The advantages of using such natural materials as a material of construction in thermal desalination units are:

- Very cheap, and available in a massive amounts in the Kingdom of Saudia Arabia.
- Light in weight which decreases the mechanical structure of the flashing stages.
- Maintenance free, because it can be replaced with new fiber with nearly free cost.
- It consists of fiber of different diameters which can improve the separation efficiency of the demister.
- Inert and can resist any chemical attack.
- Can be easily shaped to any configuration.

Figure 6. The date palm lufa and the stainless steel demisters.

Innovations:

1. Reducing the Number of Pumps [35 and 36]

In the brine circulation MSF and MEE systems, the electric power consumption amounts to 4 and 2.5 kWh/m^3, respectively. This is primarily consumed by the pumping units, The reduction of the number of pumps will decrease the number of plant trips or increase the plant availability. Breakdown of pumps and subsequent maintenance requirements represent more than 30% of trips in desalination plants. The pumps used in the MSF units are:

- The intake seawater pump.
- The cooling seawater pump.
- The distillate pump.
- The brine blow down pump.
- The brine recycle pump (only applicable for the MSF process).
- The heating steam condensate pump.
- The chemical dosing pump.

Attempts to reduce the number of pumps are proposed in a number of conceptual studies, which includes the following:

Construction of large capacity plants at 11 m elevation. This eliminates the distillate and brine blow down pumps, which in turn reduce the system capital and associated maintenance requirements of two pumps.

Use of MSF the brine circulation and thermal vapor compression or MSF-TVC. In this configuration part of the system thermal load is upgraded in the steam jet ejector rather than being disposed into the cooling seawater stream. As a result, the power rating of the cooling seawater is drastically reduced.

2. Increase the compressor capacity and the efficiency [37]

During the last two decades, the compressor capacity is increased from values below 500 m^3/d to higher values of 1000 m^3/d.

Simultaneous progress has also occurred in the compressor efficiency, where the specific power consumption of the compressor is reduced to a lower range of 6-10 kWh/m^3. The above developments resulted in reduction of the unit cost to a value of \$0.46/m^3 for MVC, which is highly competitive against the unit cost of the RO process.

3. The use of Plate and frame heat exchangers in feed water heaters [38]

The main features of the plate-to-plate heat exchanger compared to the traditional shell and tube heat exchanger include the following, Foumeny and Heggs, 1991:

- low hold-up volume (0.05-0.3 of the shell and tube system),
- close temperature approach (0.3-0.5 of the shell and tube system),
- small weight (0.1-0.3 of the shell and tube system) and small space requirements (0.25-0.3 of the shell and tube system),
- high heat transfer coefficients (1.1-1.7 higher than the shell and tube system); hence, reduced heat transfer area, and
- low fouling resistance (0.1-0.25 of the shell and tube system).

The above advantages result in reduction of the system capital and operating cost. The temperature and flow rate of the intake seawater to the plate heat exchanger is t_{cw} and M_f.

Development of MSF-TVC .[39]

As is shown in Fig. 5, separate ejectors are used to entrain and compress vapor from the last flashing chamber in the heat rejection section. Use of a single ejector is not possible, because of differences in the pressure of entrained vapor. System evaluation and analysis of the results for MSF-TVC shows the following:

- Thermal vapor compression enhances the performance of the MSF system as a result of increase in the performance ratio and reduction in the specific flow rate of cooling water and the specific heat transfer area.

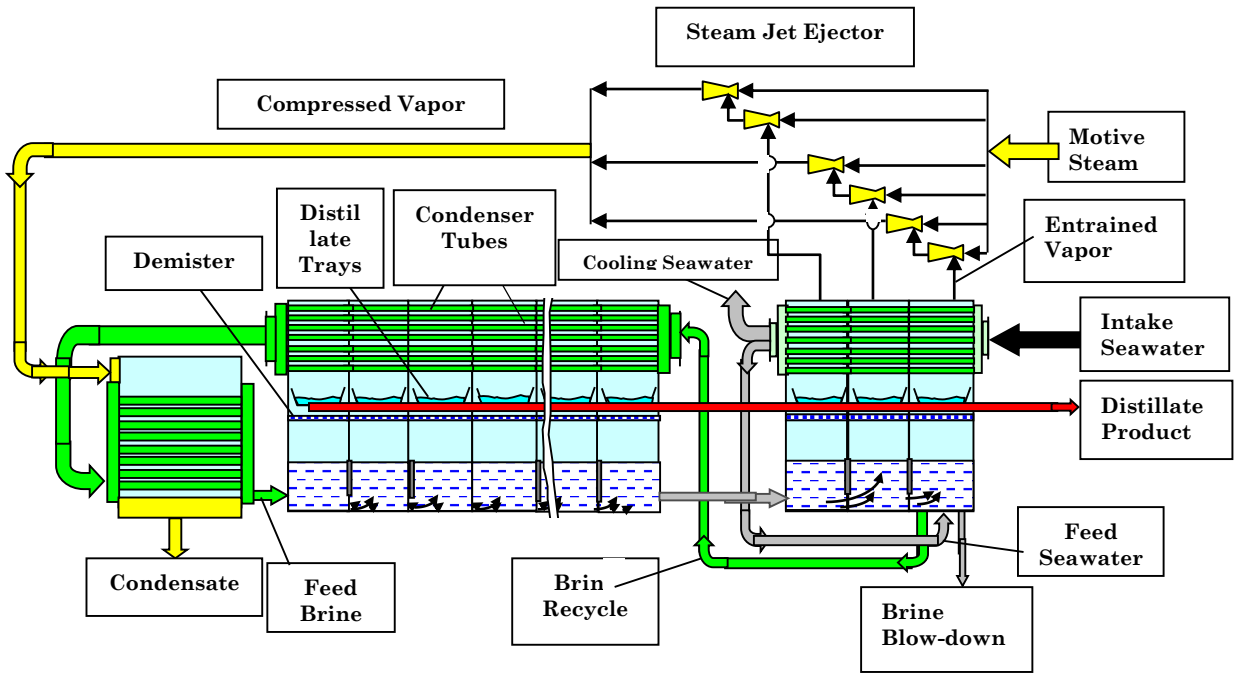

Fig. 7. Multi-Stage Flash Desalination with Thermal Vapor Compression. Mode (a) Vapor entrainment from the heat rejection stages.

Conclusions

The thermal desalination processes have gone through a large number of developments since first operation in the late 50s. These developments are achieved in the unit capacities, number of units, specific power consumption, specific unit volume, use of composite polymer materials and specific heat transfer area. As a result, drastic reduction in the unit production cost has occurred. The accumulated field experience in design, manufacturing, installation, operation, and maintenance made the thermal processes MSF process dominating the desalination market, especially thermal desalination processes. In addition, the innovations made in the design and operation of such system had a strong impact of the cost of desalination units.

Acknowledgment:

The project "Sulphur Dioxide Pollution Control and Production of Gypsum and Fresh Water" was funded by the National Plan for Science, Technology and Innovation (MAARIFAH) – King Abdul-Aziz City for Science and Technology – the Kingdom of Saudi Arabia, award number

(10-ENV-1358-08)

References

[1] Ulrich Ebensperger and Phyllis Isley, "Review of the Current State of Desalination", Water Policy Working Paper 2005-008
January 2005

[2] Emerging trends in Michelle K. Wittholz, Brian K. O'Neill, Chris B. Colby, David Lewis, "desalination: A review" , Waterlines Report Series No 9, October 2008

[3] Leitner, G., Water desalination what are today's costs, Desalination & Water Reuse, 2(1992)39-43.

[4] Bushnak, A.A., Water supply challenge in the Gulf region, Desalination, **78**(1990)133-145.

[5] Hisham T El-Dessouky, Hisham Mohamed Ettouney, "Fundamentals of salt water desalination2002, Elsevier

[6]Global Water Intelligence (2010). Water Desalination Report, 46(1).

[7]. Silver, R.S., Desalination – The distant future, Desalination, **68**(1988)1-10.[

[8]. E. Delyannis, "Historic background of desalination and renewable energies", Solar Energy 75 (2003) 357–366

[9] Hisham M Ettouney, Hisham T El-Dessouky, Imad, "Understand thermal desalination", Chemical engineering progress, 95, 9, 43-54,1999.
American Institute of Chemical Engineers

[10] deGunzbourg, J., and Larger, D., Cogeneration applied to very high efficiency thermal seawater desalination plants: A concept, Desalination & Water Reuse, 7(1998)38-41

[11] Leitner, G., Developer selected for 25 MGD (94625 m^3/d) Florida west coast seawater desalting plant, Desalination & Water Reuse, 9(1999)11-16.

[12] Pappas, C., For Cyprus 10 year "BOOT" contract, Desalination & Water Reuse, 7(1997)28-34

[13]. Zimerman, Development of large capacity high efficiency mechanical vapor compression (MVC) units, Desalination, 96(1994)51-58.

[14] Darwish, M.A., Abdel Jawad, M., and Aly, G.S., Comparison between small capacity mechanical vapor compression (MVC) and reverse osmosis (RO) desalting plants, Desalination, **78**(1990)313-326.

[15] Ettouney, H.M., El-Dessouky, H.T., Alatiqi, I., Progress in thermal desalination processes, Chemical Eng. Prog., submitted, 1998.

[16] Al-Gobaisi, D.M.K., A quarter-century of seawater desalination by large multistage flash plants in Abu Dhabi, Desalination, **99**(1994)483-508.

[17] Temperley, T.G., The coming age of desalination, Proceeding of the IDA World Congress on Desalination and Water Sciences, Abu-Dhabi, UAE, November, 1995, Vol. I, pp 219-228.

[18] Silver, R.S., Multi-stage flash distillation – The first 10 years, 3rd Int. Sym. On Fresh Water from the Sea, Athens, Greece, **1**(1970)191-206.

[19] Awerbuch, L., Perspective and challenges for desalination, Desalination, **99**(1994)191-194.

[20] Davenport, W.F., Desalination? Decision making, Desalination, 99(1994)245-255.

[21] Wangnick, K., Genthner, K., and Al-Gobaisi, D.M.K.F., The next size generation of MSF evaporators: 100,000 m^3/d, II. Design and cost aspects, material selection, Proceeding of the IDA World Congress on Desalination and Water Sciences, Madrid, Spain, October, 1997, Vol. I, pp 295-324.

[22] Rautenbach, R., and Schafer, S., Calculation of stagewise fouling factors from process data of large MSF distillers, Proceeding of the IDA World Congress on Desalination and Water Sciences, Madrid, Spain, October, 1997, Vol. I, pp 165-177.

[23] Omar, A.M., Simulation of MSF desalination plants, Desalination **45**(1983)65-67

[24] Krause, H., an -74.HM Ettouney, HT El-Dessouky, RS Faibish, and PJ Gowin, "Evaluating the economics of desalination", Chemical Engineering Progress 98 (12), 32-40

[25] H.T. El-Dessouky, H.M. Ettouney, H. Al-Fulaij, and F. Mandani, "Multistage flash desalination combined with thermal vapor compression". Chem. Eng. Proc., Vol. 39, No. 4, pp. 343-356, 2000.

[26] Noreddine Ghaffour , Thomas M. Missimer and Gary L. Amy,Technical review and evaluation of the economics of water desalination: Current and future challenges for better water supply sustainability", Desalination 309 (2013) 197–207

[27] K.V. Reddy, N. Ghaffour , "Overview of the cost of desalinated water and costing Methodologies", Desalination 205 (2007) 340–353

[28] Roberto Borsani, Silvio Rebagliati, "Fundamentals and costing of MSF desalination plants and comparison with other technologies",Desalination 182 (2005) 29–37

[29] International Atomic Energy Agency, Introduction to nuclear desalination: a guidebook, Technical Reports Series No. 400, IAEA, Vienna, Austria, 2000a.

[30] Matz, R., and Fisher, U., A comparison of the relative economics of sea water desalination by vapour compression and reverse osmosis for small to medium capacity plants, Desalination, **36**(1981)137-151.

COOLING HIGH-POWER MICROELECTRONIC DEVICES IN GROUND AND SPACE APPLICATIONS USING NANANOFIBERS AND NANOPARTICLES

Yarin A.L.*
*Author for correspondence
Department of Mechanical and Industrial Engineering, University of Illinois at Chicago, Chicago, Illinois 60607-7022, USA
E-mail: ayarin@uic.edu

ABSTRACT

The first part of the talk deals with drop/spray cooling of high-heat flux surfaces using electrospun polymer nanofiber mats. The nanofibers are copper-plated and resemble the appearance of a small Australian thorny devil lizard, i.e. became very rough (on the nano-scale), as well as acquired high thermal diffusivity. Drop impacts on the hot surfaces coated with copper-plated nanofibers revealed tremendously high values of heat removal rates up to 1 kW/(cm^2). Such high values open some intriguing perspectives for cooling of high-heat flux microelectronics and for further miniaturization of such devices, especially for such applications as UAVs and UGVs. The nano-textured coatings were tested not only in the ground (1g) experiments but also during parabolic flights at zero gravity (0g) and supergravity (1.8g). The results of the earth experiments encompass the experiments with a single needle or two needles producing drop trains or jets, with water or Fluorinert fluid FC-7300 as working fluids.

The second part of the talk deals with pool boiling on such nano-textured surfaces studied experimentally and theoretically for ethanol, water and their mixtures. The results revealed that the heat flux and heat transfer coefficient in boiling on copper-plated nano-textured surfaces were about 3-8 times higher than those on the bare copper surfaces. This stems from the fact that nano-textured surfaces promote bubble growth by increasing the average temperature of fluid surrounding growing bubbles. Hence, nano-textured surfaces facilitate bubble growth rate and increase bubble detachment frequency. On the other hand, the critical heat flux (CHF) on the nano-textured surfaces was found to be very close to its counterpart on the bare copper surfaces. However, the heat flux on the nano-textured surfaces in transition boiling was significantly higher than on the bare copper ones, since the presence of nanofibers prevented bubble merging and delayed formation of vapor film. In addition, supersonic solution blowing was used to form nano-textured copper-plated nanofiber mats with ultra-thin nanofibers of about 100 nm. In this case the pool boiling data sharply deviate from the standard boiling curve. In particular, the heat flux and the heat transfer coefficient were found to be significantly higher at low surface superheats. It was also demonstrated that the ultra-thin-nanofiber surfaces are robust and do not deteriorate after several cycles of day-long pool boiling experiments.

In the third part of the talk we explore the potential of nano-encapsulated phase change materials (PCMs) in the applications related to cooling of microelectronics using micro-channel flows. PCMs (wax or meso-erythritol) were encapsulated in carbon nanotubes by the method of self-sustained diffusion at room temperature and pressure. Such nano-encapsulated wax nanoparticles alone allow for heat removal in a relatively wide temperature range (different waxes have melting temperatures in the 40-80 C range). On the other hand, such nano-encapsulated meso-erythritol nanoparticles allow for heat removal in the 118-120 C range. The nanoparticles possess a very short response time and allow for the temperature reduction of several degrees Celsius.

NOMENCLATURE

V_i	[m/s]	The impregnation velocity
d	[m]	Pore size
a or r	[m]	Pore radius
H	[m]	Mat thickness
p	[Pa]	Pressure
x,y,X,	[m]	Cartesian coordinates
q, q	[W/cm^2]	Heat flux
V_0	[m/s]	Drop impact velocity
c	[m/s]	Speed of sound in liquid
A	[m/s^2]	Acceleration
v	[m/s]	Velocity vector
Re_a	[-]	The Reynolds number
z	[m]	Complex variable on the physical plane
h	[m]	Thickness of copper layer below the surface
T	[^{o}K]	Temperature
k	[W/(cm^{o}K)]	Thermal conductivity of copper
R	[m]	Radial cylindrical coordinate
Z	[m]	Axial cylindrical coordinate
n	[-]	Degree of fluffiness

Special characters

σ	[N/m]	Surface tension
θ	[-]	Contact angle
μ	[Pa s]	Viscosity
Π	[Pa s]	Pressure impulse
τ	[s]	The impact duration
P	[kg/m^3]	Density
ξ, η	[m]	Cartesian coordinates
φ	[m^2/s]	Potential
χ	[^{o}K]	Complex thermal potential
ω, ζ	[m]	Complex variables on the mapped plane

τ_i	[s]	The evaporation time
α	[m^2/s]	Thermal conductivity of copper
τ_t	[s]	Characteristic transition time
γ	[1/m]	Spectrum
λ	[m]	Dummy variable

Subscripts and Superscripts

a	Based on the pore radius
0	At the moment of drop impact, wetted area
s	Sample
*	Dimensional value, when specified
d	Drop
∞	The effective temperature at the copper-plated sample beyond the wetted area
w	Wetted area, Wall

INTRODUCTION

The present talk reviews the recent works conducted in The Multiscale Mechanics and Nanotechnology Laboratory at the University of Illinois at Chicago. In brief, the following topics will be addressed. Electrospinning is widely used to form polymer nanofiber mats [1]. In the present work such nanofiber mats are deposited onto high-heat flux surfaces. Even pure polymer nanofiber mats with very low thermal conductivity and the inter-fiber pores filled with air dramatically facilitate drop/spray cooling, since the prevent receding motion and bouncing of coolant droplets [2]. In addition, nanofibers can be metal-plated. Metal-plating increases thermal conductivity of nanofibers. However, the main effect of metal-plating is in the fractal-like increase of the surface roughness and area of the individual nanofibers, which significantly increases the heat removal rate and allows one to achieve the rates of cooling close to 1 kW/(cm^2) [3]. Polymer nanofiber mats facilitate cooling of high-temperature surfaces up to 300 ºC and prevent the Leidenfrost effect [4,5]. Since drop and spray cooling are considered as a realistic option for cooling of microelectronic devices onboard of Unmanned Aerial Vehicles, Unmanned Ground Vehicles (UAVs and UGVs, respectively) and space stations, nanofiber coatings for the cooling enhancement were tested in parabolic flights under the conditions of micro- and super-gravity [6,7]. The increased surface area of nanofiber mats also significantly increases the heat removal rate when cooling by the impingement air jets is used [8].

In addition to spray cooing, pool boiling is also considered as a realistic venue for cooling high-heat flux microelectronics. Metal-plated nanofiber mats significantly change the boiling curve and allow one to achieve a three- to eightfold increase in the cooling rate at low surface superheats compared to bare surfaces [9,10]. Nucleation process in liquid inside the inter-fiber pores proceeds at an increased temperature at a much higher rate, while bubble merging and formation of vapour layer is delayed or prevented by nanofibers, which cut growing bubbles and facilitate their removal by buoyancy. In such cases mechanical robustness of the nanofiber mat and its adhesion to the heater surface, as well as the ways of the improvement of mechanical properties play a decisive role.

Coolant flows through microchannels adjacent to high-heat-flux microelectronic elements open an additional attractive opportunity. Using suspensions of nanoparticles containing Phase Change Materials (PCM) attracts attention. Method of self-sustaining diffusion was developed to achieve the intercalation of different types of paraffins and meso-erythritol inside carbon nanotubes (CNTs) [11-13]. The heat transfer enhancement by means of such suspensions was investigated in [14] and revealed sufficient benefits.

ELECROSPINNING

Electrospinning of polymer solutions requires the electric field of the strength of the order of 1 kV/cm [1]. In electrospinning the electric force results in an electrically charged jet of polymer solution issued from a pendant or sessile droplet at a needle exit (cf. **Figure 1**). After such jet flows away from the droplet in a nearly straight line, it undergoes bending and coiling, which takes a form of a complex path. The electrical forces stretch and thin the jet by very large ratios, while solvent evaporates, polymer precipitates and the jet solidifies and forms nanofiber mat deposited onto a counter-electrode, or another surface attached to the counter-electrode.

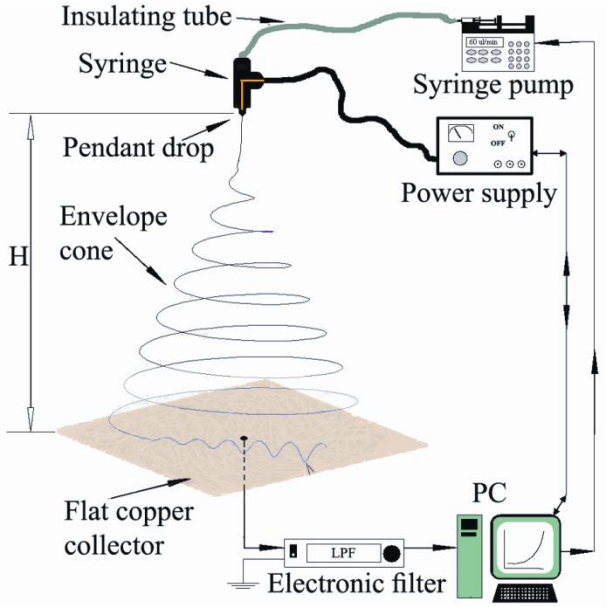

Figure 1 Schematic drawing of the electrospinning process, showing the jet path in electrospinning, and some parts of the experimental setup [15]. Courtesy of Elsevier

NANOFIBER MATS

Scanning Electron Microscopy (SEM) images of the copper-plated nanofiber mats are shown in **Figure 2**. The individual copper-plated fibers reveal thorny (**Figure 2c**) and grainy (**Figure 2d**) fractal-like nano-texture. Their surfaces are reminiscent of the Australian thorny devil lizards, which coined such fibers the name thorny-devil nanofibers [1,3] Silver-plated

nanofibers can be formed similarly and reveal predominantly dendrite-like or cactus-like structures (**Figure 3**).

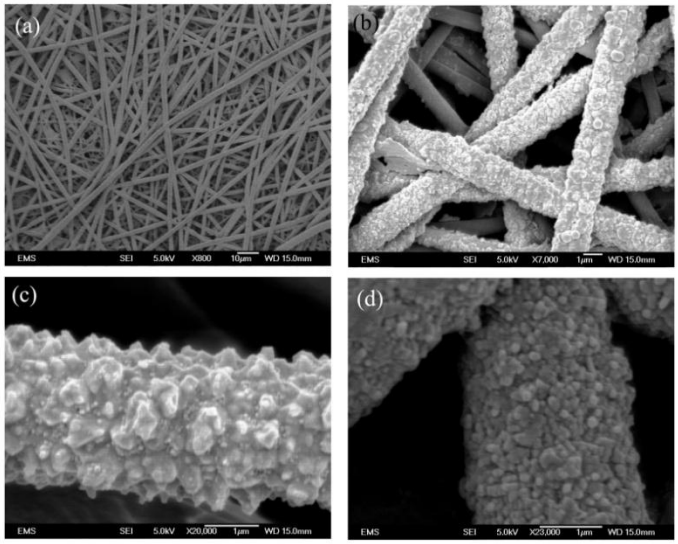

Figure 2 SEM images of the thorny devil copper-plated fibers. (a) Macroscopic view of the copper-plated fiber mat. (b) The zoomed-in view of the top layer. Several nanofibers at different locations: (c) thorny and (d) grainy nano-textures [3]. Reprinted with permission from the American Chemical Society

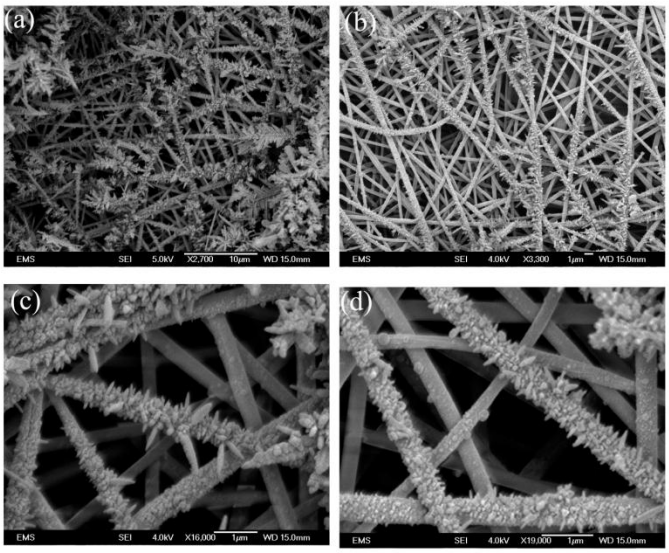

Figure 3 SEM images of the dendrite-like and cactus-like silver-plated nanofiber mats. Macroscopic views are shown in panels (a) and (b) at two different locations. The fibers look like dendrites or fern leaves in panel (a) and more cactus-like in (b). Panels (c) and (d) show zoomed-in views of cactus-like nanofibers [3]. Reprinted with permission from the American Chemical Society

DROP/SPRAY COOLING

The anti-Leidenfrost effect of metal-plated fibers is fully revealed in **Figure 4**. After the impact on a bare copper heater, the water droplet completely bounces back, which means that cooling effect is lost. On the other hand such water droplet spreads, pins itself to nanofibers, penetrates the pores by the hydrodynamic focusing mechanism, and reaches the heater surface underneath nanofibers. In spray cooling heat transfer is mostly determined by the surface area, which is dramatically enhanced due to the presence of the fractal-like nanofibers. As a result, drop evaporation time on such metal-plated mats is reduced by more than two orders of magnitude compared to that on polymer mats (50 ms in **Figure 4** for the copper-plated fibers versus 5-10 s for polymer fibers), which means that the heat flux is significantly enhanced. Namely, this then explains the tremendous cooling rate of about 1 kW/cm^2 recorded after water drop impacts onto heater surfaces with bonded 30 μm-thick copper-plated thorny devil nanofiber mats [6].

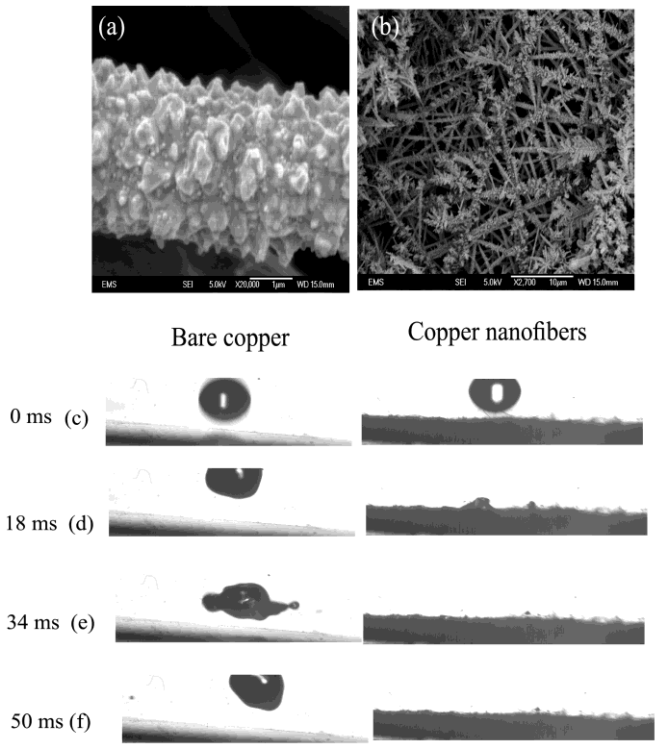

Figure 4. (a) An individual copper-plated thorny devil fiber. (b) A layer of silver-plated nanofiberes. (c)-(f) Water drop impact onto a bare copper substrate (left) and the same substrate with a bonded 30 μm-thick mat of copper thorny devil nanofibers. In both cases the surface temperature is 172.2 °C [3]. Reprinted with permission from the American Chemical Society

The experimental setup used in parabolic flights at micro- and super-gravity (0g and 1.8g, respectively) is shown in **Figure 5** and **Figure 6**.

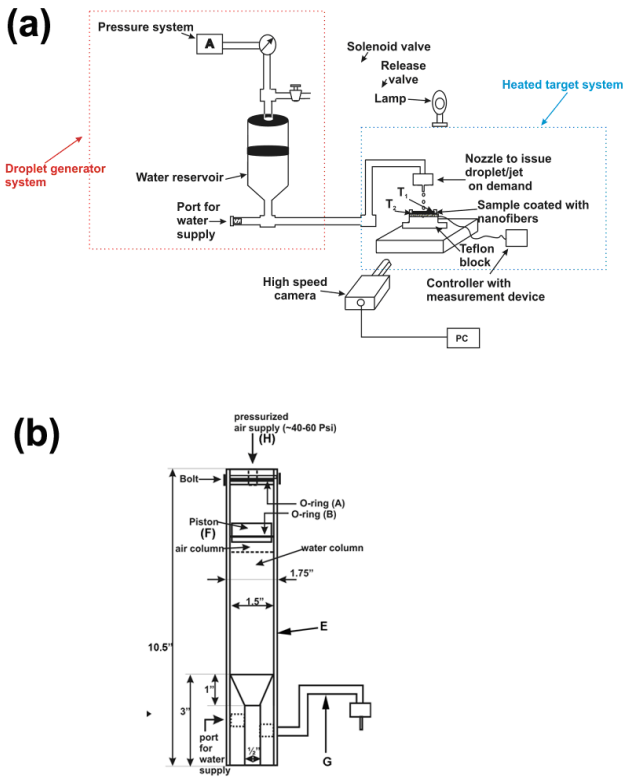

Figure 5 Schematic of the setup for cooling experiments used in parabolic flights. (a) Overall view. (b) Water reservoir [7]. Courtesy of Elsevier

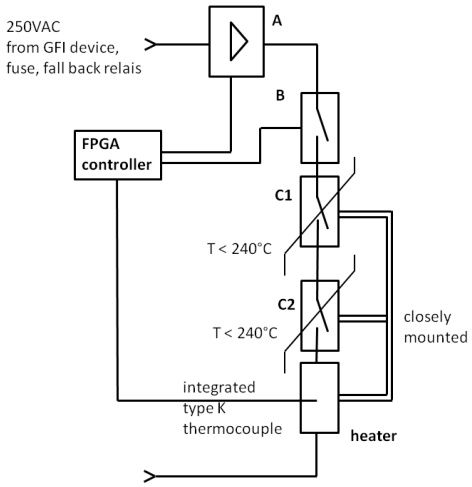

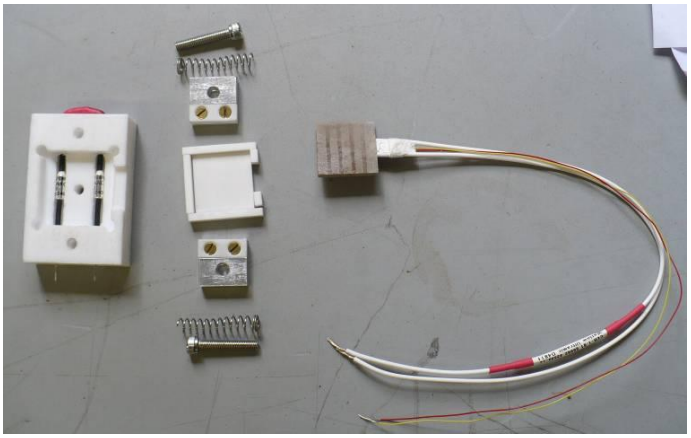

Figure 6 The heated target system (top), heated target assembly (bottom) [7]. Courtesy of Elsevier

The assembly of the setup in test camera used on board of the aircraft in parabolic flight is shown in **Figure 7** and the drop generator is detailed in **Figure 8**.

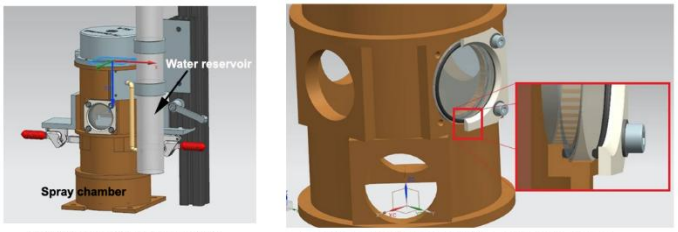

Figure 7 Schematic of the spray chamber used in the on board experiments during parabolic flights [7]. Courtesy of Elsevier

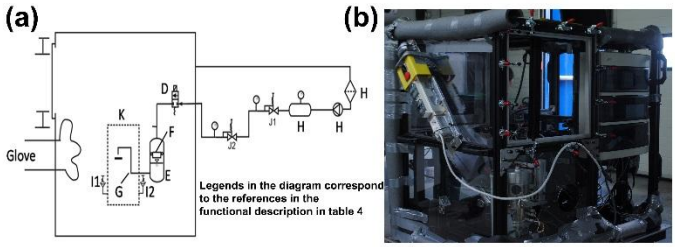

Figure 8 Droplet generator, the spray chamber and enclosure: (a) Schematic. (b) Drop generator used in the parabolic flight experiments [7]. Courtesy of Elsevier

Several representative images of water drops after impacts onto nanofiber-coated heaters in parabolic flights under different conditions are shown in **Figure 9**.

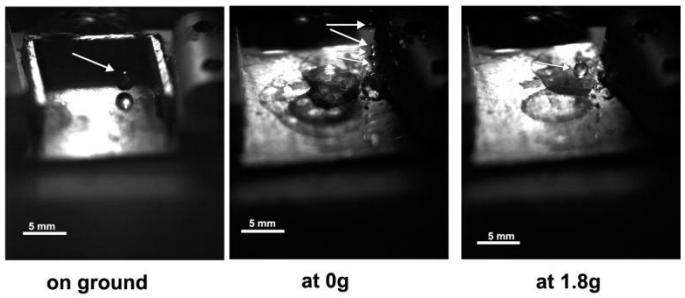

Figure 9 Water drops issued from the droplet generator under different gravity conditions. On the on ground and under super-gravity (1.8g) the generator produced single drops. On the other hand, in micro-gravity a stream of tiny water droplet was produced. The droplets are highlighted by arrows [7]. Courtesy of Elsevier

In the parabolic flight experiments, a single drop was issued onto the targets from the droplet generator (see **Figure 10**). The further developments, namely, drop impact, spreading and evaporation were recorded using a high-speed camera. This allowed us to measure the evaporation time and the effective wetted area. Using such information, the heat flux removed from the surface was calculated in one of the methods applied. In **Figure 10** three different snapshots of a single water drop impact onto a bare copper (**Figure 10a**) and onto a copper-plated nanofiber mat surface (**Figure 10b**) are shown at t=0, t=400 ms and t=679 ms. At the moment t=679 ms the water drop has already evaporated on the copper-plated nanofiber mat. However, the water drop had not evaporate yet on the bare copper surface at this moment. The heat flux corresponding to these images was found to be 61.31 W/cm^2 for bare copper surface and 124.45 W/cm^2 for the copper-plated nanofiber mat. It should be emphasized that in the present experiment, in distinction from [3], the target was not located on top of a large hotplate kept at a constant temperature. The large size of the heater in [3] provided a practically infinite heat source for a single drop experiment. In the parabolic flight experiments, however, the area of the heater was 1 in^2, which was same as the sample area, while the heater thickness was small. Therefore, in the parabolic flight experiments the heater did not serve as an infinite heat source like the large hotplate in [3]. In addition, for the safety-related reasons according to the ESA regulation, in the parabolic flight experiments the heater was kept at a low output (with the maximum output being ~ 200-250 W) and the temperature sampling frequency was ~40-60 ms. All the above-mentioned factors together resulted in a smaller heat supply rate in comparison to that of [3], and accordingly, in a smaller heat removal rate. It should be emphasized that no Leidenfrost effect was observed on bare copper in parabolic flight experiments in distinction from the experiments in [3]. This stems from the fact that in the parabolic flights the heater had a lower thermal capacity and a limited output, as well as the sampling rate was slower in the present case. However, the trends in the main results were the same in the parabolic flight experiments and in the ground experiments in [3], i.e, the heat removal rate was much higher on the copper-plated nanofiber mats than on the bare copper substrate.

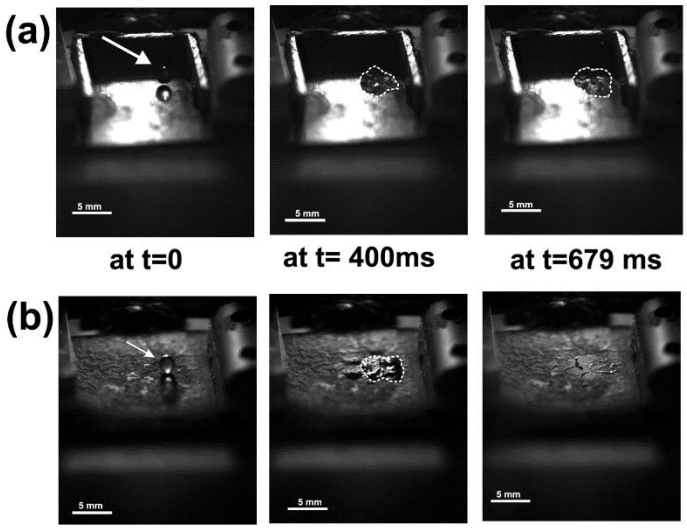

Figure 10 High-speed images of water drop impact and evaporation on: (a) a bare copper substrate, and (b) a copper-plated nanofiber mat at 125 ºC. Three different time moments are shown. It is easy to see that the water drop evaporates much faster on the copper-plated nanofiber mat than on the bare copper substrate. The impinging drops are highlighted by arrows and the wetted areas on the surfaces are traced by dashed lines [7]. Courtesy of Elsevier

THEORETICAL: HYDRODYNAMIC FOCUSING AS THE MECHANISM OF ENHANCEMENT OF DROP/SPRAY COOLING THROUGH NANOFIBER MATS

Liquid brought softly to the nanofiber mat surface can impregnate pores if the nanofiber mat surface is partially wettable. The speed of wettability-driven impregnation of pores is given by, $V_i \sim \sigma d \cos\Theta/(8\mu H)$, where H is the pore length and its permeability is taken as $a^2/8$ as in the Hagen-Poiseuille flow, with d being the pore diameter and $a = d/2$ its radius. The advancing contact angle is denoted as Θ, which is less than $\pi/2$ in this case. On the other hand, non-wettable pores can be filled in a static situation (when liquid softly comes into contact with pores) if the pressure difference between the liquid at the pore entrance and gas inside Δp is larger than the Laplace pressure, i.e. $\Delta p > -2\sigma\cos\Theta/d$, with $\Theta > \pi/2$ in this case. In the case of drop impact $\Delta p = \rho V_0^2/2$. It is easy to see that with $|\cos\Theta| \sim 1$, non-wettable mats with pores $d = 10^{-3}$cm would not be filled with water at impact speeds of the order of 1-2 m/s, since the static inequality does not hold. Indeed, the ratio of the right hand side to the left hand side in this inequality is of the order of 10 and the static condition predicts no filling of non-wettable nanofiber mats. However, it does not account for the dynamic nature of the impact filling process (the hydrodynamic focusing

effect), which is responsible for the rapid filling of semi-wettable or non-wettable nanofiber mats in the experiments in the present work. The dynamic nature of the pore filling process after drop impact on porous media manifests itself according to the following scenario.

In our experiments drop sizes are typically of the order of $D \sim 10^{-2} - 10^{-1}\,\mathrm{cm}$, whereas the pore sizes are of the order of d~10^{-3} cm. Therefore, drop impact onto a single pore can be imagined as an abrupt impact of a solid wall with an orifice in the middle onto an upper half-space filled with water (see **Figure 11)**. To be able to apply the calculation technique

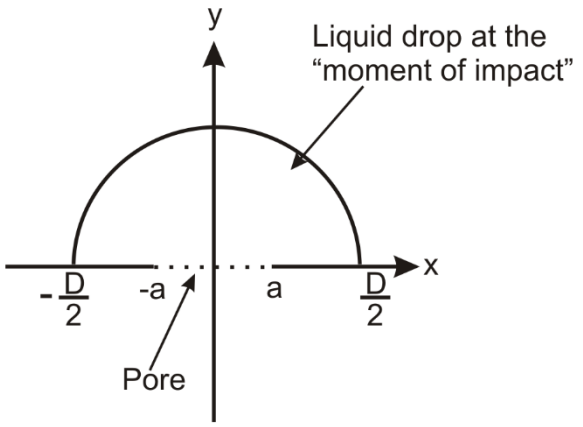

Figure 11 Sketch of a drop impact onto a single pore [16]. Courtesy of Elsevier

rooted in the Cauchy formula of the complex analysis, consider a kindred two-dimensional problem. Namely, a plane at *y* = 0 with a slit in the middle at $-a < x < a$ (where a = d/2 is analogous to the pore radius) imposes a pressure impulse on the liquid filling the upper half-plane y > 0. The pressure impulse $\Pi = \lim\limits_{\substack{\tau\to 0\\ p\to\infty}} \int_0^\tau \Delta p\,dt$ (where pressure $\Delta p \to \infty$ and the impact duration $\tau \to 0$) is of the order of one. The pressure impulse is applied at $-\infty < x \le -a$, y = 0 and $a \le x < \infty$, y = 0 to the liquid filling the upper half-plane. Flows arising in response to the pressure impulse are known to be potential, with flow potential $\varphi = -\Pi/\rho$ being a harmonic function [17,18]. The value of the pressure impulse corresponding to drop impact can be evaluated as follows. Assume first that liquid in the drop comes to rest after an impact on a solid obstacle as fast as the pressure waves in it related to its compressibility deliver the information from the preceding layers (as it happens at the very first moments after an impact). Then, the convective part of the normal force acting on the obstacle is of the order of $\rho V_0 c D^2$, where c is the speed of sound in the liquid. In addition, the "water hammer" part of normal force acting on the obstacle related to the deceleration is of the order of $-\rho D^3 A$, where the liquid acceleration is of the order of $A = -V_0 c / D$. Therefore, the "water hammer" part of the normal force acting on the obstacle is also of the order of $\rho V_0 c D^2$. Hence, the pressure from the liquid experienced by the obstacle, as well as the pressure which the drop bottom experiences from the obstacle, are of the order of $\Delta p \sim \rho V_0 c$. If one assumes that liquid comes to rest after a certain spreading, then the short-living compressibility effects can be neglected, the normal load at the wall due to the dynamic pressure is of the order of $\rho V_0^2 D^2$ and the "water hammer" load is of the same order, since in this case $A = -V_0 / (D/V_0)$. Thus, in the latter case the pressure which the drop bottom experiences from the obstacle is of the order of $\Delta p \sim \rho V_0^2$, much less than in the compressible case. However, due to the fact that in the compressible case $\tau \sim D/c$, whereas for the latter incompressible stage $\tau \sim D/V_0$, the value of the pressure impulse $\Pi \sim \rho V_0 D$ is the same irrespective of the deceleration mechanism. Therefore, the potential value in liquid in contact with the wall is

$\varphi(X) = \varphi_0 = -V_0 D$ over $-\infty \le X \le -a$, y=0 and $a \le X \le \infty$, y=0 (1)

$\varphi(X) = 0$ over $-a < X < a$, y=0 (2)

The distribution of the potential (a harmonic function) in the liquid filling the upper half-plane is found using the Cauchy formula, which in the present case inevitably reduces to Poisson's integral formula for the upper half-plane [19]

$$\varphi(x,y) = \frac{1}{\pi}\int_{-\infty}^{\infty} \frac{\varphi(X,0)\,y}{(x-X)+y^2}\,dX \tag{3}$$

The integral in Eq. (3) is evaluated using Eqs. (1) and (2) and the resulting flow potential needed to calculate the flow through the opening is given by

$$\varphi(x,y) = -\frac{\varphi_0}{\pi}\arctan\left(\frac{2ay}{x^2+y^2-a^2}\right) \tag{4}$$

The corresponding velocity vector is $\mathbf{v} = \nabla\varphi$. Therefore, the y-component of **v** over the opening $-a < x < a$ is found as

$$v_{\text{opening}}(x) = \left.\frac{\partial\varphi}{\partial y}\right|_{y=0} = \frac{V_0 D}{\pi}\frac{2a}{x^2-a^2} \tag{5}$$

Note that $v_{\text{opening}} < 0$. Therefore, as expected, after drop impact, liquid begins to flow into the opening, i.e. in the negative y-direction. At the opening edges, at $x = \pm a$, $v_{\text{opening}} = -\infty$, since there the pressure impulse is discontinuous. This is typical for problems of penetration of solid plates into an incompressible liquid [17]. In reality, the velocity at the orifice edges will be diminished by viscosity due to the no-slip condition, which is excluded from the consideration in the present analysis. However, it can still be expected that liquid penetration into the orifice will take the

shape of an upside down corona. The velocity minimum is expected at the opening center, where $\left|\left(V_{opening}\right)_{min}\right| = U$, with U given according to Eq. (5) by

$$U = \frac{4}{\pi}\frac{D}{d}V_0 \qquad (6)$$

A more detailed calculation based on the conformal mapping of the drop domain to the upper half-plane is possible, as illustrated in **Figure 12** [19]. This reveals that the same Eq. (6) is valid in the limit D/d>>1.

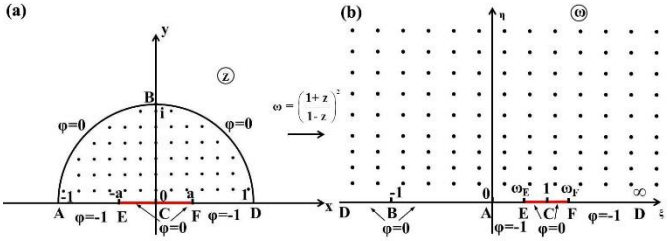

Figure 12 Conformal mapping onto the upper half-plane [16]. Courtesy of Elsevier

The x-component of the velocity vector over the opening vanishes, i.e. the flow through it right after the drop impact will be strictly anti-parallel to the *y* axis. The central part of the flow through the opening will not be affected by viscous forces if $\rho U^2 >> \mu U/a$, which is equivalent to the condition that the Reynolds number based on the half-width of the opening $Re_a = \rho U a/\mu >> 1$. Taking for the estimate $D \sim 10^{-2} - 10^{-1}$ cm, $d = 2a = 10^{-3}$ cm and $V_0 \sim 1$ m/s, we find that $U \sim 10 - 10^2$ m/s $>> V_0$ and for water $Re_a = 10^2 - 10^3$. Therefore, in this case the high value of U will not be affected by viscosity even for such small pores, even though the flow close to the opening or orifice edges will be affected by viscosity. This analysis can be extended, in principle, to the case when drop penetrates simultaneously several pores, which will diminish the value of U. Still, a large disparity between D and d will result in U >> V_0.

The high values of the velocity U compared with drop impact velocity V_0 stem from accumulation and channeling of the kinetic energy of a large mass of liquid in flow through a narrow orifice. This is the manifestation of the phenomenon known as hydrodynamic focusing [16]. Similar phenomena are responsible for the formation of shaped-charge (Munroe) jets. It is emphasized that similar high velocities related to geometry-dictated accumulation and channeling of kinetic energy were previously predicted and observed in the incompressible drop impacts on liquid layers, where such high-speed jets appear near the bottom part of the drop.

The predicted values of the flow velocity through the orifice $U \sim 10 - 10^2$ m/s can also be compared with the speed of wettability-driven impregnation of pores $V_i \sim \sigma d \cos\Theta/(8\mu H)$ mentioned above. Taking for the estimate $H \sim 10^{-2}$ cm and $d = 10^{-3}$ cm, we obtain for water $V_i \sim 1$ m/s, i.e. $V_i << U$. Therefore, the accumulation and channeling effect dominates wettability and can lead to dynamic filling of pores even in completely non-wettable porous media. Only at the latter quasi-static stage, would water tend to leave such non-wettable porous materials, even though some separated blobs can stay there forever.

Note that an axisymmetric problem on drop impact onto a single pore was also solved in [4]. It revealed the initial velocity of liquid penetration into a single pore as

$$U = 2\frac{D}{d}V_0 \qquad (7)$$

As expected, in the axisymmetric case (7), the value of U is even higher than that for the planar case of Eq. (6).

DIRECT EXPERIMENTAL OBSERVATION OF HYDRODYNAMIC FOCUSING

Since the drop sizes D are much larger than the pore sizes d, direct measurements of the initial velocity of liquid penetration into the pores U at the ratios D/d>>1 are challenging (since they involve sizes of the order of 1-10 μm and times of about 0.1 ms). Such measurements were undertaken for the first time in our recent work [16], and the corresponding result is shown in as shown in **Figure 13**.

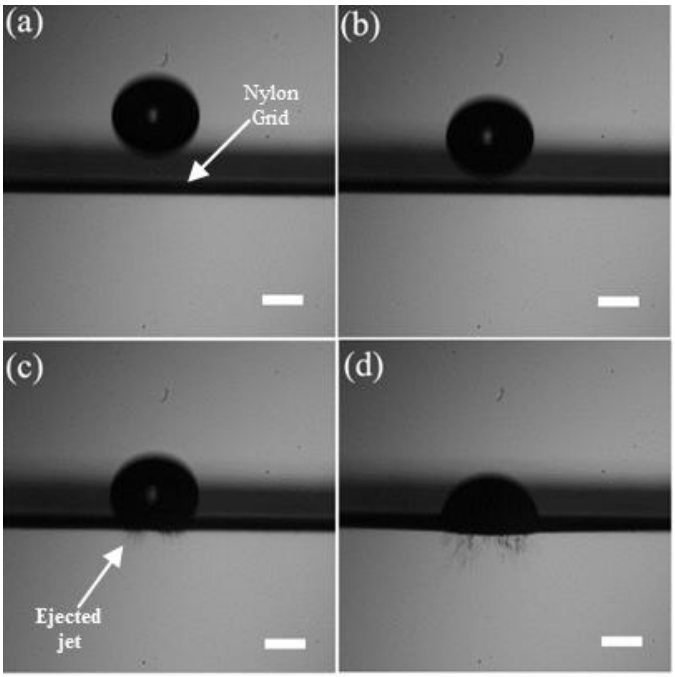

Figure 13 Impact of a Fluorinert fluid FC 7500 drop onto a nylon grid of thickness 60 μm with an impact velocity of 2.1 m/s. The images correspond to (a) t = 0 μs, (b) t = 200 μs, (c) t = 400 μs and (d) t = 600 μs. Scale bars, 1mm. The drop size is D=2 mm [16]. Courtesy of Elsevier

Nylon grid of pore size 6 μm was used to elucidate the hydrodynamic focusing effect. The drop impact was recorded by a high-speed camera at 10,000 fps. The velocity of the drop at the moment of impact was 2.1 m/s. The velocity of a jet ejected through several holes in the grid in **Figure 13c** was measured as 6.77 m/s. The velocity of the jet was measured by the distance the jet travelled within a frame of recording, i.e. during 100 μs. It should be emphasized that even though the velocity in the jet, which passed not through a single but about 160 pores, was decelerated by viscous friction with the pore walls and slightly damped by the nylon grid oscillation during the impact, was still 3.25 times higher than the impact velocity V_0. This shows that the initial penetration velocity through a single pore U>6.77 m/s. According to the axisymmetric result discussed in the preceding section, Eq. (7), $U = 2(D/d)V_0 = 1.3\times10^3$ m/s through a single pore (approximately, about 8 m/s in the case of 160 pores). The density and surface tension of the Fluorinert fluid used (FC 7500) are ρ=1.614 g/cm^3 and σ=16.2 g/s^2, respectively. Therefore, in the present case the ratio $(\rho V_0^2)/(4\sigma/d) = 0.66$, and penetration of liquid in the pores happened below the static penetration threshold due to hydrodynamic focusing.

THEORETICAL: TEMPERATURE FIELD AND HEAT TRANSFER ACCOMPANYING DROP IMPACT ONTO A SINGLE PORE

Planar Problem. Consider a planar problem on the temperature field in a sample cooled by a drop array impinging onto its surface. For a single droplet impact, it takes about τ_i=0.07 s to evaporate water on a copper sample surface, as the experimental data discussed above show. If one is interested in the thermal field in a copper layer of thickness h below the surface, the characteristic time of reaching a steady-state thermal field there would be of the order of $\tau_t=h^2/\alpha$ where α is the thermal conductivity of copper (α=1.12 cm^2/s). Taking for the estimate h=2 mm, we obtain τ_t=0.036 s. Since $\tau_t < \tau_i$, even for cooling by a single droplet the thermal field in the sample can be assumed being steady. In the case of a multi-droplet cooling, when a liquid puddle at the surface appears, the thermal field in the sample is steady as well. When the temperature field in the sample is steady, it satisfies the planar Laplace equation (a planar two-dimensional case is considered in this sub-stection). The temperature at the entire surface of the sample is given and equal to T_s everywhere except a section of the surface $y^*=0$ where the impact takes place, where at $-r \le x^* \le r$ the temperature is equal to T_d which is lower than T_s (the dimensional coordinates are denoted by asterisk as a superscript), as depicted in **Figure 14a**. It is convenient to consider the modified temperature function (the potential) $\varphi^*=-k(T^*-T_s)$ where k is the thermal conductivity of the sample material (the dimensional potential and temperature are denoted by asterisk as a superscript). Note, that $\varphi^* \le 0$. This function obviously satisfies the planar Laplace equation. It is equal to zero everywhere at the sample surface except the section $-r \le x^* \le r$, $y^*=0$ where it is given as $\varphi_0=-k(T_d-T_s)>0$. The sample domain is assumed to fully occupy the domain $y^* \ge 0$.

The solution of the planar Laplace equation for the function φ^* is given by Poisson's integral formula for the upper half-plane [19] which reduces to the following expressions for the above-mentioned boundary conditions

$$\varphi^*(x,y) = \frac{1}{\pi}\int_{-r}^{r} \frac{\varphi^*(X^*,0)y^*}{(X^*-x^*)^2+y^{*2}}dX^* = \frac{\varphi_0}{\pi}\int_{-r}^{r} \frac{y^*}{(X^*-x^*)^2+y^{*2}}dX^* \quad (8)$$

where X^* is the dummy variable.

Evaluating the integral in Eq. (8), we obtain

$$\varphi^*(x^*,y^*) = \frac{\varphi_0}{\pi}\arctan\left(\frac{2ry^*}{x^{*2}+y^{*2}-r^2}\right) \quad (9)$$

Rendering φ^* dimensionless with φ_0, and x^* and y^* dimensionless with r, we reduce Eq. (9) to the following dimensionless form

$$\varphi(x,y) = \frac{1}{\pi}\arctan\left(\frac{2y}{x^2+y^2-1}\right) \quad (10)$$

where the dimensionless parameters do not have superscripts (asterisk), and, in particular, $\varphi=(T^*-T_s)/(T_d-T_s) \ge 0$. Denote $S = x^2+y^2-1$. It is easy to see that for S<0, the branches of the arctangent in Eq. (10) should be chosen as follows: for S<0, $\pi/2 \le \arctan(S) \le \pi$, whereas for S>0, $0 \le \arctan(S) \le \pi/2$.

The dimensionless heat flux is found from the Fourier law as $\mathbf{q} = \nabla\varphi$ (since the minus sign is included in the definition of φ). The heat flux is rendered dimensionless by $\varphi_0/r>0$. Its projections q_x and q_y found from the differentiation of Eq. (8) read

$$q_x(x,y) = \frac{2y}{\pi}\int_{-1}^{1} \frac{(X-x)}{\left[(X-x)^2+y^2\right]^2}dX \quad (11)$$

$$q_y(x,y) = \frac{1}{\pi}\int_{-1}^{1} \frac{1}{(X-x)^2+y^2}dX - \frac{2y^2}{\pi}\int_{-1}^{1} \frac{1}{\left[(X-x)^2+y^2\right]^2}dX \quad (12)$$

Evaluating the integrals in these equations, we find

$$q_x = -\frac{4xy}{\pi\left[(1-x)^2+y^2\right]\left[(1+x)^2+y^2\right]} \quad (13)$$

$$q_y = -\frac{(1-x)\left[(1+x)^2+y^2\right]+(1+x)\left[(1-x)^2+y^2\right]}{\pi\left[(1-x)^2+y^2\right]\left[(1+x)^2+y^2\right]} \quad (14)$$

The dimensionless temperature field φ and the fields of the components of the heat flux q_x and q_y given by Eqs. (10), (13) and (14) are plotted below **in Figures 14b-16**, respectively. It should be emphasized that at the cooling surface y=0, a discontinuity of the temperature is imposed at $x = \pm 1$. Therefore, in the planar problem the heat flux components have infinite magnitudes at y=0 and $x = \pm 1$, as follows from Eqs. (13) and (14). The values of q_x and q_y at y=0 are not included in **Figures 15** and **16**. The overall heat removal rate through the surface y=0 and $x = \pm 1$ appears to be infinite in the planar problem, as well, which is a direct consequence of the simplification of the boundary condition. Nevertheless, for the general structure of the fields of interest in the sample domain it is rather immaterial, and **Figures 14-16** give a clear picture of the sample cooling in the case of interest.

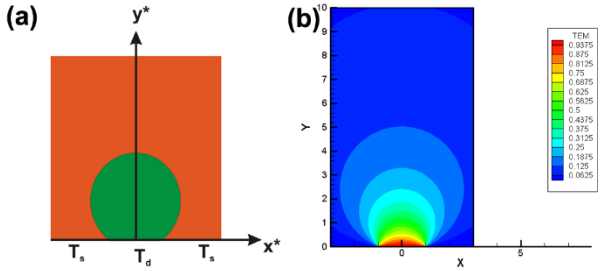

Figure 14 (a) Sketch of a drop on the surface. (b) Dimensionless temperature field φ [6]. Courtesy of Elsevier

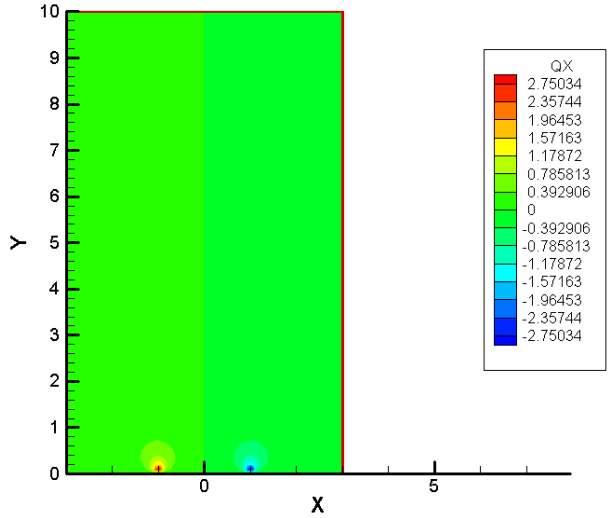

Figure 15 The field of the q_x component of the heat flux [6]. Courtesy of Elsevier

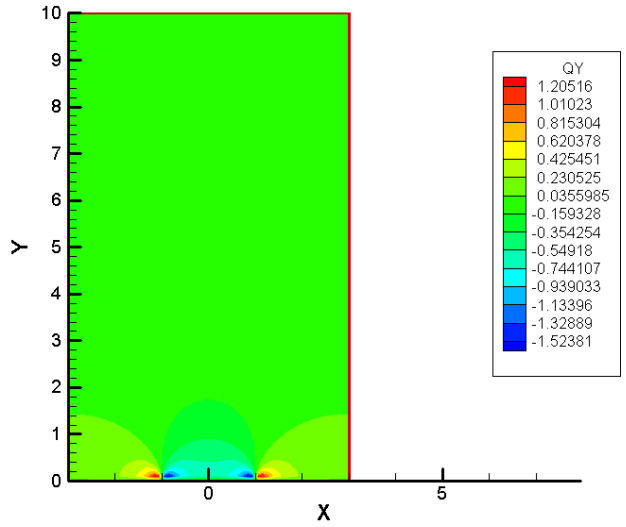

Figure 16 The field of the q_y component of the heat flux [6]. Courtesy of Elsevier

Axisymmetric Problem. It is of significant interest to consider the axisymmetric thermal problem corresponding to drop cooling. In this case the Laplace equation for the temperature field in the sample reads

$$\frac{1}{R}\frac{\partial}{\partial R}\left(R\frac{\partial T}{\partial R}\right)+\frac{\partial^2 T}{\partial Z^2}=0 \quad (15)$$

where R is the radial coordinate, Z is the vertical axis, and T is the temperature. It should be emphasized that only the dimensional parameters are used here and hereinafter in this sub-section, and therefore, there is no special notation (superscript asterisk) for them. Here, the origin of the coordinate system is fixed at the center of surface of a nanofiber-coated sample, and the positive direction of Z is taken into the sample towards the hotplate. The boundary conditions are posed as follows

$$T\big|_{Z=0} = f(R) \quad (16)$$

$$T\big|_{R=0} < \infty \quad (17)$$

$$T\big|_{\substack{R\to\infty \\ Z\to\infty}} < \infty \quad (18)$$

The function f(R) is determined by a given temperature distribution at the sample surface discussed below.

Using separation of variables, the solution for the temperature field is found as it

$$T(R,Z) = \int_0^\infty \exp(-\gamma Z) J_0(\gamma R)\gamma\left[\int_0^\infty f(\lambda)\lambda J_0(\gamma\lambda)d\lambda\right]d\gamma \quad (19)$$

where γ represents the continuous spectrum of the present problem, J_0 is the Bessel function of the first kind of zero order, and λ is a dummy variable.

Similarly to the planar problem the temperature distribution at the sample surface is assumed to be discontinuous and taken as

$$f(R)=\begin{cases}T_0, & R<a_w\\ T_\infty, & R>a_w\end{cases} \tag{20}$$

where T_0 is the temperature of the wetted area, a_w is the effective radius of the wetted area, and T_∞ is the effective temperature at the copper-plated sample beyond the wetted area.

Equations (19) and (20) yield the following temperature distribution at the symmetry axis R=0

$$T\big|_{R=0}=T_\infty+(T_0-T_\infty)\left[1-\frac{Z}{\sqrt{Z^2+a_w^2}}\right] \tag{21}$$

Using Eq. (21) the heat flux at the sample surface is found as

$$q_{axis}=\left|-k\frac{\partial T}{\partial Z}\right|_{Z=0}\Bigg|=k\frac{(T_\infty-T_0)}{a} \tag{22}$$

where k is the conductivity of the sample [for copper k=4 W/(cm ºK)].

POOL BOILING ON NANO-TEXTURED SURFACES

Pool boiling on nano-textured surfaces formed by copper-plated electrospun nanofibers was recently studied experimentally and theoretically in [9,10]. The experimental setup used is sketched in **Figure 17**. The boiling patterns observed on bare copper surface and on the copper-plated nano-textured surface are presented in **Figure 18**, and the corresponding results for the heat flux, surface superheat and the heat transfer coefficient are shown in **Figure 19** and **Figure 20**. The dramatic increase in the heat removal rate corresponds to an increased temperature in liquid bulk inside the inter-fiber pores where nucleation takes place, which is facilitated by a higher and higher fluffiness of the nanofiber mat, as the theoretical results shown in **Figure 21** reveal.

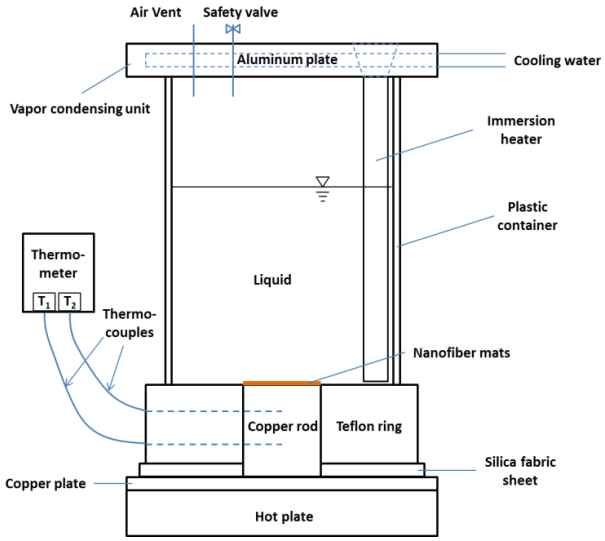

Figure 17 Sketch of the experimental setup used in pool boiling experimental setup. In some cases an immersion heater was inserted as shown to facilitate boiling [9]. Courtesy of Elsevier

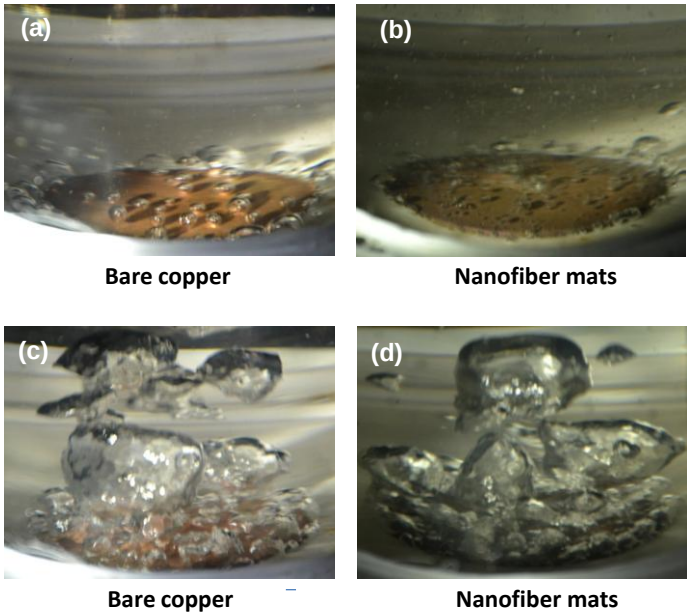

Figure 18 Pool boiling of water on the bare copper surfaces and surfaces coated with copper-plated nanofiber mats at the heater temperature of 200 ºC in panels (a,b) and 400 ºC in panels (c,d) [9]. Courtesy of Elsevier

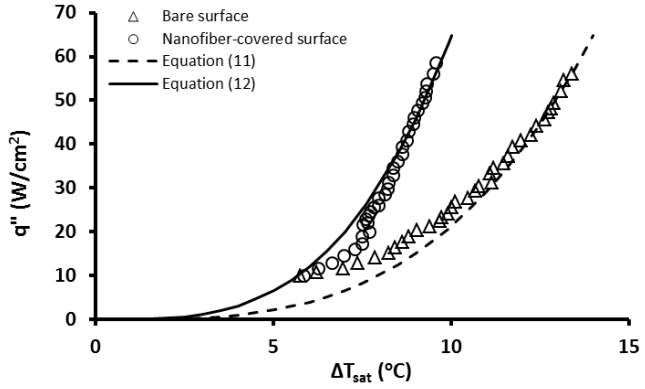

Figure 19 Heat removal rate for boiling of water on a smooth bare copper surface and copper-plated nanofiber mat [9]. Courtesy of Elsevier

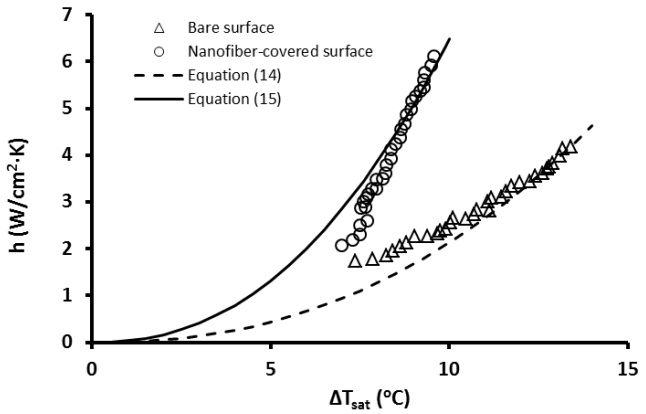

Figure 20 Heat transfer coefficient measured on a smooth bare copper surface and copper-plated nanofiber mat [9]. Courtesy of Elsevier

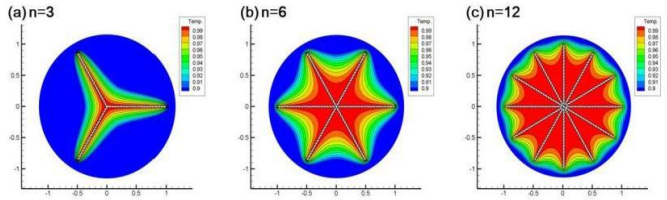

Figure 21 Temperature fields predicted at different degrees of model nanofiber mat fluffiness [9]. Courtesy of Elsevier

The temperature field in **Figure 21** was clalculated using the following approach. Consider the temperature field in liquid in contact with a hot wall assuming that it is in steady state and governed by the planar Laplace equation. We assume that the wall is isothermal and had periodic protrusions into liquid in the form of star shapes representing nanofiber mats of different degree of fluffiness n, as shown in **Figure 22**.

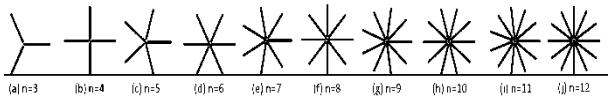

Figure 22 Nanofiber mat morphologies of different degree of fluffiness n [9]. Courtesy of Elsevier

A generic star-like shape mimicking nanofiber mat fluffiness is shown in **Figure 23a**. The dotted liquid domain in the physical plane of the complex variable z=x+iy (with x and y being the Cartesian coordinates and i the imaginary unit) surrounding the star-like structure can be conformally mapped onto the dotted upper half-plane in the ζ- plane (**Figure 23b**; ζ=ξ+iη) by the following mapping function

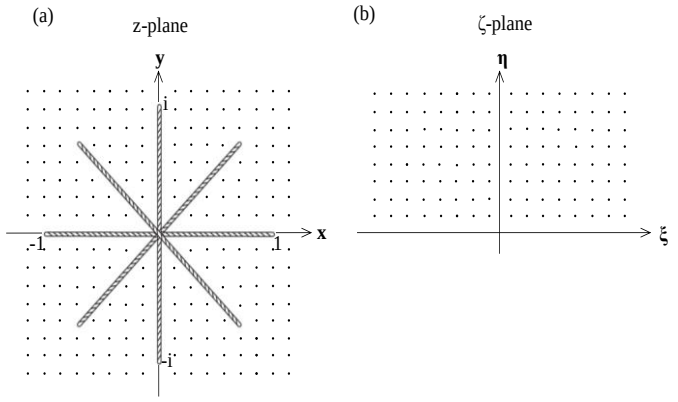

Figure 23 (a) Conformal mapping of the area in the physical plane z surrounding the star-like fluffy structure onto (b) the upper half-plane ζ [9]. Courtesy of Elsevier

$$z = \frac{1}{\sqrt[n]{4}} \frac{\left\{\left[(i-\zeta)/(i+\zeta)\right]^n + 1\right\}^{2/n}}{(i-\zeta)/(i+\zeta)} \tag{23}$$

where the degree of fluffiness n is a positive integer.

In the ζ-plane the temperature distribution is one-dimensional

$$T(\xi,\eta) = T_w - \frac{qL\eta}{k} \tag{24}$$

where T_w is the wall temperature, k is the thermal conductivity of liquid, L is the length scale, and q is the heat flux.

The temperature field (A2) satisfies the planar Laplace equation. Therefore, we can introduce the analytic complex thermal potential

$$\chi = \psi(\xi,\eta) + iT(\xi,\eta) \tag{25}$$

with the real part ψ being related to the imaginary part (temperature) T via the Cauchy-Riemann conditions

$$\frac{\partial\psi}{\partial\xi} = \frac{\partial T}{\partial\eta}, \quad \frac{\partial\psi}{\partial\eta} = -\frac{\partial T}{\partial\xi} \tag{26}$$

Combining Eqs. (24) and (25), we find the complex thermal potential in the ζ- plane as

$$\chi(\zeta) = iT_w - \frac{qL}{k}\zeta \tag{27}$$

On the other hand, Eqs. (27) and (23) allow one to find the complex thermal potential in the z-plane χ(z) and its imaginary part T(x,y), which represents temperature field about the star-like fluffy structures of **Figure 22**, when their rays are sustained at the wall temperature T_w and the heat flux at infinity is q. The temperature fields produced by Eqs. (27) and (23) are illustrated in **Figure 21**.

COOLING USING MICROCHANNEL FLOWS WITH PCM-CONTAINING CARBON NANOTUBES

The method of self-sustaining diffusion developed in [11,12] and illustrated in **Figure 24** allows one to intercalate carbon nanotubes (CNT) with polymers, surfactants and nanoparticles at room temperature and pressure.

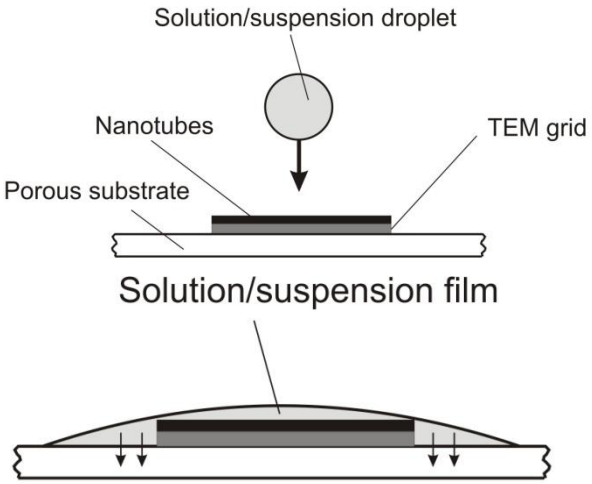

Figure 24 Sketch of the experimental procedure used in the method of self-sustained diffusion. (Top) Polymer/surfactant/nanoparticles/other solutes are delivered in a gently deposited droplet, while a layer of nanotubes rests on top of a lacey carbon TEM grid. (Bottom) The small vertical arrows indicate absorbance of the solution/suspension by the porous substrate, which creates a thin film. This film is rapidly depleted of solvent due to evaporation. Solvent evaporation in this film concentrates the solute, and thus sustains its diffusive flux toward the CNT open ends [12]. Reproduced with permission from The Royal Society of Chemistry

This method was employed in [13, 14] to intercalate such Phase Change Materials (PCM) as paraffins (waxes) and meso-erythritol inside carbon nanotubes. The intercalated CNTs are shown in the Transmission Electron Microscopy (TEM) images in **Figure 25**.

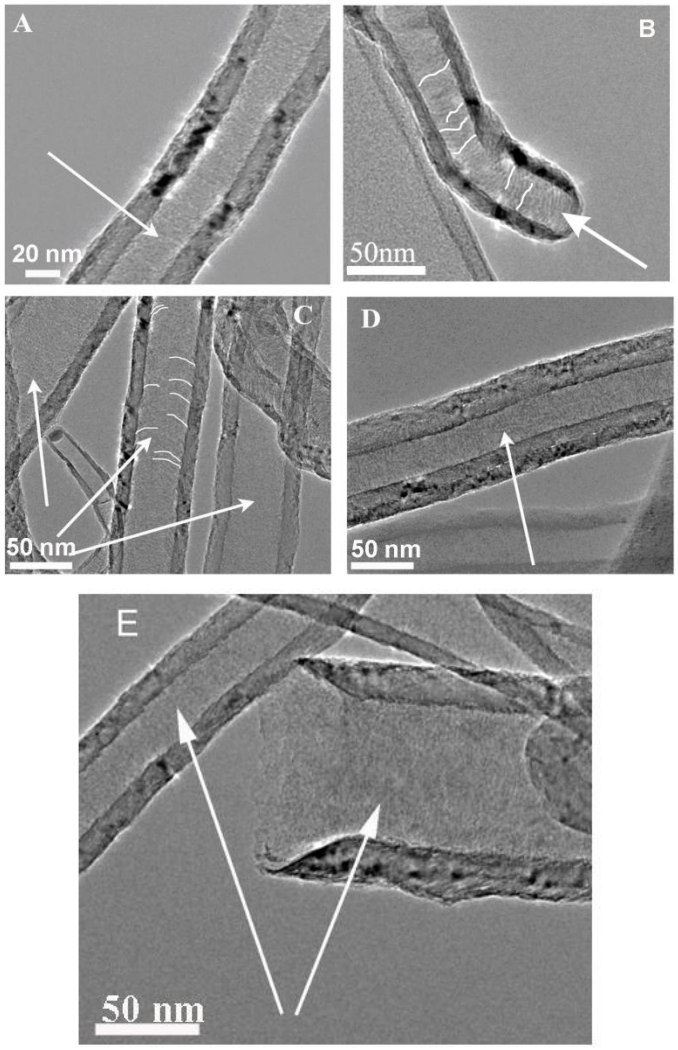

Figure 25 TEM micrographs of CNTs intercalated by different waxes are shown in panels A-E. The arrows point at the striations that can be seen inside the deposits in the CNTs. The waxes are deposited only inside the tubes, with no residual wax visible outside. Several characteristic striations are highlighted in panels B and C [13]. Reproduced with permission from The Royal Society of Chemistry

Such PCM-intercalated CNTs were suspended in carrier fluids (water or oil) and used in flows through mictrochannels inserted into a heater body, as sketched in **Figure 26**.

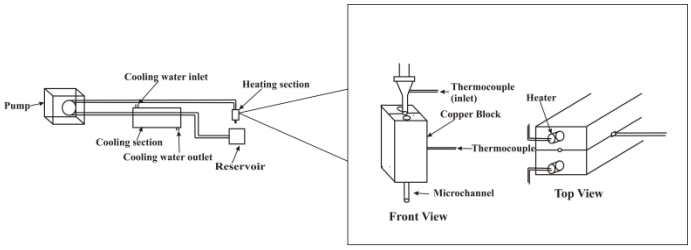

Figure 26 Schematic of the experimental setup used to study heat removal using microchannel flows of wax-intercalated or meso-erythritol-intercalated CNTs [14]. Reproduced with permission from The Royal Society of Chemistry

The experimental results on the measured reduction of the heater temperature due to flow of a 3% suspension of empty or wax-intercalated CNTs are shown in **Figure 27**. These results allow one to elucidate the contribution of the intercalated PCM (wax, in the present case) to the reduction of the heater (copper block) temperature. It should be emphasized that surfactants are added to stabilize solutions and affect the flow rate. The data in **Figure 27** allow separation of this effect from that of the PCM and the standard "wind chill" effect.

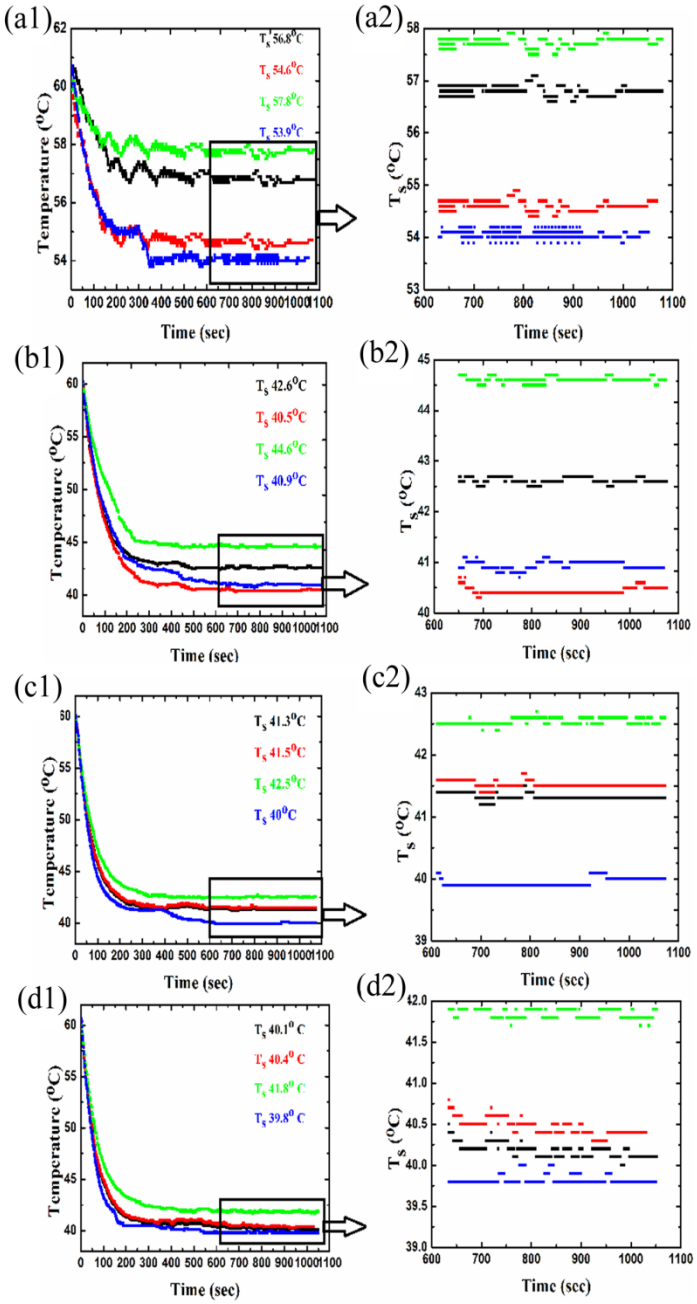

Figure 27. Temperature of the copper block versus time in the case of flows of water, surfactant solution, 3 wt% suspension of the empty CNTs, and 3 wt% of wax-intercalated CNTs in 1803 μm channel. The panels show the temperature histories corresponding to the following rates of the coolant flow: (a1) and (a2) correspond to the flow rate of 5 ml/min, (b1) and (b2) – to 25 ml/min, (c1) and (c2) – to 45 ml/min, (d1) and (d2) – to 55 ml/min. The panels marked with numeral 1 correspond to the transient phase, whereas those marked with numeral 2 – to the subsequent steady-state stage**.** Black symbols correspond to pure water, red symbols - to the aqueous surfactant solution, green symbols - to the aqueous suspension of the empty CNTs, and blue symbols - to the aqueous solution of wax-intercalated CNTs. The values of the steady-state temperature reached are

shown by the corresponding colors. For the experiments at the flow rate of the 5 ml/min the inlet coolant temperature was 23.6 °C, whereas for the other experiments it was 20.2 °C. The rectangular domains in the left-hand side panels corresponding to the steady-state regimes are shown in detail in the right hand side panels [14]. Reproduced with permission from The Royal Society of Chemistry

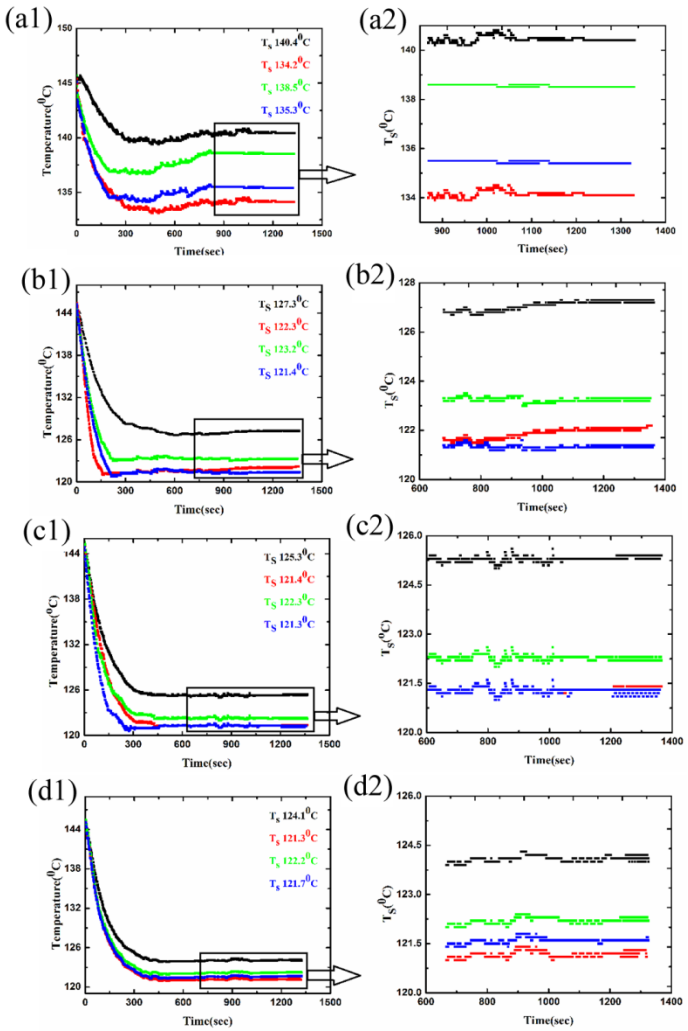

Figure 28 Temperature of the copper block versus time in the case of flows of oil, oil-based surfactant solution, 1.5 wt% suspension of the empty CNTs, and 1.5 wt% of erythritol-intercalated CNTs in the 1803 μm channel. The panels show the temperature histories corresponding to the following rates of the coolant flow: (a1) and (a2) correspond to the flow rate of 25 ml/min, (b1) and (b2) – to 45 ml/min, (c1) and (c2) – to 55 ml/min, (d1) and (d2) – to 65 ml/min. The panels marked with numeral 1 reveal the transient phase, whereas those marked with numeral 2 – the subsequent steady-state stage**.** Black symbols correspond to pure oil, red symbols - to the oil-based surfactant solution, green symbols - to the oil-based suspension of the empty CNTs, and blue symbols - to the oil-based suspension of the erythritol-intercalated CNTs. The values of the steady-state temperature achieved are shown by the corresponding colors. For the experiments the inlet coolant temperature was 24.6 °C. The rectangular domains in the left-hand side panels corresponding to the steady-state regimes are shown in detail in the right-hand side panels [14]. Reproduced with permission from The Royal Society of Chemistry

The measured temperature drop (in comparison to the suspension of the empty CNTs) due to the erythritol melting in CNTs in steady-state regimes for different flow rates revealed the following results: for the flow rates of 25, 45, 55 and 65 ml/min, ΔT = 3.2 °C, 1.8 °C, 1 °C and 0.5 °C, respectively (cf. **Figure 28**). These results show that the longer residence time in the channel maximized the erythritol melting and its cooling effect.

In addition note that the oil-based suspensions of the empty CNTs had practically the same cooling effect as the pure oil due to the balancing the effect of the surfactant induced-slip by the increased viscosity due to the CNT presence.

CONCLUSION

In drop/spray cooling experiments with nano-textured heater surfaces covered by electrospun copper-plated nanofibers the values of the heat removal rate close to 1 kW/cm^2 were achieved at normal gravity. Safety regulations did not allow using the heater to its full capacity during the parabolic flights, therefore the heat removal rate could not be as high as in the ground experiments. As a result of this heater limitation the maximum achievable heat removal rate was thus diminished. Under the flight conditions the heat removal rate was in the range 200-338 W/cm^2 for zero gravity (0g), normal gravity (1g) [the flights setup] and super-gravity (1.8g). In all cases the copper-plated nanofibers removed heat much better than bare copper. The heat removal rate achieved due to the copper-plated nanofibers during the parabolic flights was 2 to 5 times higher than that for bare copper.

In pool boiling experiments under the ground gravity conditions nano-textured copper surfaces coated with copper-plated nanofiber mats revealed a 6-8 times higher heat flux and heat transfer coefficient in nucleate boiling of ethanol in comparison with the corresponding values measured at bare copper surfaces. For the nucleate boiling of water, the heat flux and heat transfer coefficient on nano-textured surfaces is 3-5 times higher than those of bare copper surface. The superiority of nano-textured surfaces in comparison to the bare surfaces is attributed to the fact that the effective temperature in liquid in the vicinity (in the inter-fiber pores) of such fluffy surfaces is higher than near the smooth surfaces. The high heat removal rates are achieved at low surface superheats, which means that nano-textured surfaces have significant benefits for surface cooling compared to that of smooth surfaces.

In the experiments with microchannel flows the results show that wax-intercalated and erythritol-intercalated carbon nanotubes (CNTs) hold promise as phase change materials (PCM) for cooling microelectronics using coolant suspension. The presence of wax inside CNTs additionally facilitated heat removal through the latent heat of wax fusion. Wax melted in

the range 45-47 °C and this effect alone was responsible for the maximum temperature reduction of 1.9 °C. The heat removal due to wax melting is diminished at the highest flow rates, since the CNT residence time inside the 3.175 cm-long channel became too short for wax melting.

The presence of erythritol inside CNTs additionally facilitated heat removal through the latent heat of its fusion in flows of the oil-based suspensions. The erythritol melted in the 118-120 °C range and this effect alone was responsible for the maximum temperature reduction of 3.2 °C in flows of the oil-based 1.5 wt% suspension of erythritol-intercalated CNTs.

Mixtures of different PCMs, e.g. wax and erythritol (separately in different CNTs, or together in the same CNTs) can be used to widen the temperature range of PCM-related cooling in some applications, if needed.

The support of this work by NASA (Grant No. NNX13AQ77G) and NSF (Grant CBET 1133353) is greatly appreciated. Contributions of my PhD students Suman Sinha-Ray, Yiyun Zhang, Sumit Sinha-Ray, Seongchul Jun and Rakesh Sahu, as well as collaboration with several groups from Technical Universitat Darmstadt, Korea University, North Carolina State University and Worcester Polytechnic Institute, are acknowledged.

REFERENCES

[1] A.L. Yarin, B. Pourdeyhimi, S. Ramakrishna, *Fundamentals and Applications of Micro- and Nanofibers*, Cambridge University Press, Cambridge, 2014

[2] Srikar R., Gambaryan-Roisman T., Steffes C., Stephan P., Tropea C., Yarin A.L. Nanofiber coating of surfaces for intensification of spray or drop impact cooling, *International Journal of Heat and Mass Transfer*, Vol. 52, 2009, pp. 5814-5826

[3] Sinha Ray S., Zhang Y., Yarin A.L. Thorny devil nano-textured fibers: The way to cooling rates of the order of 1 kW/cm^2, *Langmuir*, Vol. 27, 2011, pp. 215-226

[4] Weickgenannt C.M.,Zhang Y., Lembach A.N., Roisman I.V., Gambaryan-Roisman T., Yarin A.L., Tropea C. Non-isothermal drop impact and evaporation on polymer nanofiber mats, *Physical Review E*, Vol. 83, 2011, 036305

[5] Weickgenannt C.M., Zhang Y., Sinha-Ray S., Roisman I.V., Gambaryan- Roisman T., Tropea C., Yarin A.L.. The inverse-Leidenfrost phenomenon on nanofiber mats on hot surfaces, *Physical Review E*, Vol. 84, 2011, 036310

[6] Sinha-Ray S., Yarin A.L. Drop impact cooling enhancement on nano-textured surfaces. Part I: Theory and results of the ground (1g) experiments, *International Journal of Heat and Mass Transfer*, Vol. 70, 2014, pp. 1095-1106

[7] Sinha-Ray S., Sinha-Ray S., Yarin A.L., Weickgenannt C.M., Emmert J., Tropea C. Drop impact cooling enhancement on nano-textured surfaces, Part II: Results of the parabolic flight experiments [zero gravity (0 g) and supergravity (1.8 g)], *International Journal of Heat and Mass Transfer*, Vol. 70, 2014, pp. 1107-1114

[8] S. An, C. Lee, M. Liou, H. S. Jo, J.-J. Park, A. L. Yarin, S. S. Yoon. Supersonically blown ultra-thin thorny devil nanofibers for efficient air cooling, *ACS Applied Materials & Interfaces*, Vol. 6, 2014, pp. 13657-13666

[9] Jun S., Sinha-Ray S., Yarin A.L.. Pool boiling on nano-textured surfaces, *International Journal of Heat and Mass Transfer*, Vol. 62, 2013, pp. 99-111

[10] Yang L., Patel V., Seyed-Yagoobi J., Jun S., Sinha-Ray S., Zhang Y., Yarin A. Enhancement of nucleate boiling heat transfer with nanofiber mat, *Proceedings of the ASME 2012 Summer Heat Transfer Conference HT2012-58107*, July 8-12, 2012, Rio Grande, Puerto Rico, pp. 1-9, 2012

[11] A.V. Bazilevsky, K. Sun, A.L. Yarin, C.M. Megaridis, Selective intercalation of polymers in carbon nanotubes, *Langmuir*, Vol. 23, pp. 7451-7455

[12] A.V. Bazilevsky, K. Sun, A.L. Yarin, C.M. Megaridis, Room-temperature, open-air, wet intercalation of liquids, surfactants, polymers and nanoparticles within nanotubes and microchannels, *Journal of Materials Chemistry*, Vol.18, 2008, pp. 696 – 702

[13] R. Sahu, S. Sinha-Ray, A.L. Yarin, B. Pourdeyhimi, Drop impacts on electrospun nanofiber membranes, *Soft Matter* Vol. 8, 2012, pp. 3957-3970

[14] S. Sinha-Ray, S. Sinha-Ray, H. Sriram, A.L. Yarin, Flow of suspensions of carbon nanotubes carrying phase change materials through microchannels and heat transfer enhancement, *Lab-on-a- Chip*, Vol. 14, 2014, pp. 494-508

[15] S.A.Theron, E. Zussman, A.L. Yarin, Experimental investigation of the governing parameters in the electrospinning of polymer solutions, *Polymer* Vol. 45, 2004, pp. 2017-2030

[16] R.P. Sahu, S. Sett, A.L. Yarin, B. Pourdeyhimi, Impact of aqueous suspension drops onto non-wettable membranes: hydrodynamic focusing and penetration of nanoparticles, *Colloids and Surfaces A: Physicochemical and Engineering Aspects*, Vol. 467, 2015, pp. 31-45

[17] G.K. Batchelor, *An Introduction to Fluid Dynamics*, Cambridge University Press, Cambridge, 1981

[18] N.E. Kochin, I.A. Kibel, N.V Rose, *Theoretical Hydrodynamics*, Interscience Publishers, New York, 1964

[19] G. Polya, G. Latta, *Complex Variables*, Wiley, New York, 1974